Vapor mixing in turbulent vaporizing flows

L. Germes Martinez, Benjamin Duret, J. Reveillon, F.X. Demoulin

To cite this version:

L. Germes Martinez, Benjamin Duret, J. Reveillon, F.X. Demoulin. Vapor mixing in turbulent vaporizing flows. International Journal of Multiphase Flow, 2023, 161, pp.104388. 10.1016/j.ijmultiphaseflow.2023.104388 . hal-03934207

HAL Id: hal-03934207
https://hal.science/hal-03934207

Submitted on 24 Jan 2023

Vapor mixing in turbulent vaporizing flows

L. Germes Martinez, B. Duret*, J. Reveillon, F.X. Demoulin

CORIA-UMR 6614 - Normandie Université, CNRS-Université et INSA de Rouen, Campus Universitaire du Madrillet, 76800 Saint Etienne du Rouvray, France.

Abstract

Scalar mixing and evaporation processes are analyzed in a compressible two-phase homogeneous and isotropic turbulence configuration. To this end, the fully compressible Navier-Stokes equations are solved using a pressure-based method and a mass-conservative interface capturing method (CLSVOF). Temperature and vapor mass fraction transport equations are coupled with the momentum equation via the evaporation rate: i.e. heat and mass transfer has an effect on the flow dynamic through the generation of a Stefan flow at the interface. In this formalism, a pressure equation is developed to include the acoustic, thermal dilatation and compressibility effects. Moreover, the method can consider several gas structures in the same domain, each with independent temperature, density, and thermodynamic pressure. The latter is important to simulate atomization, where interaction among the liquid structures (such as breakup or coalescence) can generate multiple gas inclusions. This work is one of the first to describe with high fidelity the vaporization and turbulent mixing occurring in dense two-phase flows.

A statistical analysis of the vapor mass fraction field is performed. The obtained results reveal the influence of the non-homogeneous scalar source at the interface, which depend directly on the local interface temperature, on the PDF shape. Under these conditions, the vapor mass fraction PDF deviates from the Gaussian and beta PDF shapes, frequently used for turbulent combustion modeling. Furthermore, access to the local surface averaged vapor mass fraction and

---

*Corresponding author : duret@coria.fr

Preprint submitted to International Journal of Multiphase Flow *January 24, 2023*

evaporation rate at the interface allows a statistical analysis of these variables. Results show a large dispersion of both quantities, especially at the early times of the simulations, which contradict the usual assumption of a constant vapor mass fraction (or vaporization rate) at the interface used in the literature in standard vaporization models. Finally, the influence of the mean interface curvature on the evaporation rate is quantified and discussed. Large evaporation rate are present when the interface is convex (positive mean curvature). On the contrary, local saturation zones are present near concave interface (negative mean curvature), reducing the evaporation rate magnitude.

Keywords: DNS, Compressible, Turbulent mixing, Two-phase flows,
Evaporation, CLSVOF

This is a draft version, the peer reviewed and most recent version is available in IJMF :
`https://doi.org/10.1016/j.ijmultiphaseflow.2023.104388`

1. Introduction

Mixing and evaporation have a significant role in many natural and engineering processes. For instance, the performance and pollutant emissions of internal combustion engines depend highly on these two processes. Generally, mixing is enhanced by a turbulent flow, when compared with a process driven mainly by diffusion. The ability of these flows to increase the surface between the fluids intensifies the molecular diffusion (Dimotakis, 2005). An example of the importance of turbulent mixing in nature is the release of pollutants (such as chemicals, solid particles, or heat) into the atmosphere or aqueous environments.

Furthermore, in industry, turbulent mixing is the driving mechanism for heat and mass transfer in a chemical reactor, especially in cases where the turbulent and reaction time scales are comparable. During the mixing process, three distinct stages can be identified (Eckart, 1948). First is the initial state, in which the entrainment of one fluid into another occurs. This is characterized by large concentration gradients at the interface and a near-zero gradient elsewhere. In the intermediate state, the motion created by the larger eddies distorts the interface and increases molecular transport between the fluids. As the fluids become more homogeneous at the final state, the concentration gradients decrease until there is no more heat or mass transfer.

Normally, scalar mixing in turbulent flows is studied with different strategies depending on how the scalar is released into the carrier phase (Hunt, 1985). For instance, in experiments the scalar is released as a single point source in the flow by adding a relatively small amount of dye to a liquid. Such scenarios have been studied in an experimental framework using the evolution of single-point and two-point statistics of the scalar fields.

Experimental measurements of the probability density function (PDF) of a passive scalar in a homogeneous turbulent shear flow performed by Tavoularis and Corrsin (1981) indicated a quasi-normal distribution for the scalar signal. Subsequently, several experimental and theoretical works show that, under certain conditions, the scalar PDF, with a mean scalar gradient, exhibits an exponential tail due to anomalous mixing (Shraiman and Siggia (1994); Chertkov et al. (1998); Pumir et al. (1991)). Moreover, Jayesh and Warhaft (1992) studied the evolution of the scalar PDF and the dissipation rate for passive temperature fluctuations in decaying grid-generated turbulence; concluding that the scalar PDF has a pronounced exponential tail for turbulence Reynolds number (Re_λ) above 70 but below this value the PDFs can be modeled by a normal distribution.

Several authors have also resorted to direct numerical simulations (DNS) to investigate passive scalar mixing in turbulent flows. For example, Eswaran and Pope (1988) used DNS to study the mixing of a passive scalar in an isotropic turbulent flow. Here, the authors observed the effect of the initial conditions on the temporal evolution of the scalar rms and the scalar dissipation rate. Additionally, they analyzed the evolution of the scalar PDF shape from a double-Dirac function distribution to a Gaussian distribution. Similar simulations were carry out by Overholt and Pope (1996); Juneja and Pope (1996); Yeung (2001). Furthermore, Yeung et al. (2002) used DNS of isotropic and homogeneous turbulence to investigate the effects of the Schmidt number on the inertia and dissipation length scales of the scalar energy spectrum. More recently, Yeung et al. (2005) studied a 2048^3 DNS of passive scalar mixing in a turbulent flow, observing a deviation from small-scale isotropy. Yeung and Sreenivasan (2013, 2014) used DNS to study the mixing of passive scalars with a very low Schmidt number; the goal was to confirm the existence of the $-17/3$ power law of the scalar spectral density in the inertial-diffusive range.

In turbulent combustion modeling, one way for approximating the local averaged chemical production rate is the use of a presumed scalar PDF. In this method, the scalar pdf shape is assumed *a priori*, and the parameters of such PDF are determined by solving the transport equation of the first couple of moments (Girimaji (1991)). The PDFs commonly used for this purpose are the Gaussian (Lockwood and Naguib (1975)) and the beta-pdf (Gerlinger (2003); Lempke et al. (2015)). An example is the work of Gerlinger (2003), which performs simulations of a supersonic hydrogen-air diffusion flame assuming the multivariable beta-pdf proposed by Girimaji (1991). A major drawback of this approach is that the PDF shape is chosen from a mathematical perspective instead of a physical one. To improve this method, Bray et al. (2006) investigated the accuracy of predicting the mean reaction rate in turbulent premixed flames using three presumed pdf: beta-pdf, twin delta function, and a pdf based on unstrained flame properties. They found a large deviation with the first two assumed PDFs compared with DNS calculations. Similar results were found by Salehi and Bushe (2010) when simulating a premixed flame with an assumed beta-pdf approximation and a modified laminar flamelet PDF.

More recently, a new approach was proposed by de Frahan et al. (2019). Machine learning techniques were used to develop assumed PDF models for reacting flows. When comparing the proposed method with a standard beta pdf model, significant improvements were found. Furthermore, Lipatnikov et al. (2021) used the PDF directly extracted from DNS and presumed beta-function using the first two moments yielded by DNS data for modeling the combustion process variable and the mean source term in a premixed turbulent flame.

The studies mentioned above on passive scalar mixing in a turbulent flow use a single-phase configuration. In most cases, the scalar source is defined during the simulation initialization as one or several vapor patches arbitrarily distributed in the domain. However, scalar mixing has been studied using a Lagrangian approach to account for the two-phase flows. An example is the work of Reveillon and Demoulin (2007), where the effect of the droplet's spatial distribution on evaporation and scalar mixing is investigated. They use a spectral DNS solver for the evolution of the turbulent carrier phase and a Lagrangian model for the dispersed phase, which acts as scalar point sources. Several publications focus on the study of turbulent mixing in similar scenarios (Reveillon et al. (1998); Demoulin and Borghi (2002); Colin and Benkenida (2003)). The main interest of this type of work is to understand the effect of the vaporization source term in the scalar transport equation on the evolution of the mean vapor mass fraction, fluctuations and dissipation rate.

A limitation when using the point-particle Lagrangian approximation is that the simulations are restricted to particles smaller than the Kolmogorov scale. A fully resolved DNS coupled with an interface capturing method must be performed to simulate larger particles. This type of configuration was adopted by Duret et al. (2012). They studied the mixing process in a two-phase HIT configuration with a vaporizing liquid. Statistical and spectral analysis were presented to demonstrate the effects of liquid volume fraction on the velocity and scalar fields. Nevertheless, this work does not consider the coupling between vaporization rate and flow dynamics through the velocity jump condition at the interface. Consequently, the study is limited to low vaporization rates, where the phase change process hardly affects the interface and flow dynamics. Bouali et al. (2016) used a similar setup to study the influence of the liquid/gas interfaces on the scalar dissipation rate statistics.

In the literature, several numerical strategies include the relation between temperature, vapor mass fraction and fluid dynamics in their formalism (Esmaeeli and Tryggvason, 2004; Tanguy et al., 2007; Malan, 2018; Palmore Jr and Desjardins, 2019; Scapin et al., 2020). Since the conservation equations are coupled through the interface jump conditions, the above methods can be subdivided according to the interface representation used. To implement one of these methods to study the scalar mixing and vaporization processes in a turbulent and confined environment, the effect of compressibility must be considered in order to conserve the initial total mass. A step toward this kind of simulation was taken by Scapin et al. (2021) and Dodd et al. (2021), who used a low-mach formulation of the Navier-stokes equations. Consequently, the gas density is a function of pressure and temperature in their simulations. However, this formalism considers a spatially constant thermodynamic pressure, which could affect the result if more than one gas structure is present in the domain. To overcome this limitation, a fully compressible formulation of the Navier-Stokes equations, where the acoustic and compressibility effect are resolved, could be used. For instance, the method proposed by Urbano et al. (2022) is a good candidate for this type of simulation. They use a semi-implicit projection method to solve the compressible Navier-Stokes equations coupled with cubic equations of state, which allows them to consider real fluid interactions. However, mass transfer is not yet implemented in their formalism.

In this work, the all-Mach formalism proposed by Martinez et al. (2021) is used to study the scalar mixing and evaporation process. To this end, a two-phase HIT configuration with phase change is considered. In this formalism, the interface velocity jump is handled explicitly during the resolution of the compressible Navier-Stokes equations, and the interface regression induced by the liquid evaporation is taken into account using a sink term in the VOF transport equation. Consequently, the Stefan flow and its effect on the system dynamics are captured. Moreover, the momentum, energy, and species conservation equations are coupled by the evaporation rate present in the jump conditions, resulting in a non-homogeneous temperature and vapor mass fraction at the interface. Another consequence of the coupling among the conservation equations is that the scalar is not passive since its eventual variation will directly affect the turbulent velocity field. For the reasons mentioned above, the description of the physical phenomena in our work could be considered a major step forward compared with the available publications in the literature. Moreover, this study is considered as an important evolution of our previous study which used a passive scalar to model vaporization (Duret et al., 2012). Such improvement of the description of phase change has been achieved with the development of numerical methods pursued in the last decade in our team.

In the following, the governing equations, jump conditions, and numerical methods are first described. The numerical configuration is then explained alongside the initial simulation parameters. Then, a statistical analysis of the vapor mass fraction and evaporation rate is performed based on the temporal evolution of the mean, variance and PDFs of both variables. Ultimately, the role of the interface curvature on the vaporization rate magnitude is discussed by analyzing their joint PDF.

2. Governing equations

This work considers a two-phase flow composed of a monocomponent liquid and a mixture of ideal gases. Both phases are fully compressible and are separated by an infinitely thin interface, where heat and mass transfer occurs. The gas phase is initially described as dry air. When evaporation starts, the inert air mixes with the vapor generated around the interface. The system of equations solved for both phases is the following:

$$\begin{cases} \dfrac{\partial \rho}{\partial t} + \boldsymbol{\nabla} \cdot (\rho \boldsymbol{u}) = 0 & \text{(1a)} \\ \dfrac{\partial \rho \boldsymbol{u}}{\partial t} + \boldsymbol{\nabla} \cdot (\rho \boldsymbol{u} \otimes \boldsymbol{u}) = \boldsymbol{\nabla} \cdot \bar{\bar{\Omega}} + \sigma H \delta_\Gamma \boldsymbol{n} + \rho \boldsymbol{f_{vol}} & \text{(1b)} \\ \rho c_p \left(\dfrac{\partial T}{\partial t} + \boldsymbol{u} \cdot \boldsymbol{\nabla} T \right) = \boldsymbol{\nabla} \cdot (\lambda \boldsymbol{\nabla} T) + \alpha_T T \dfrac{\mathrm{D}P}{\mathrm{D}t} & \text{(1c)} \\ \dfrac{\partial Y_v}{\partial t} + \boldsymbol{u} \cdot \boldsymbol{\nabla} Y_v = \dfrac{\boldsymbol{\nabla} \cdot (\rho_g D_m \boldsymbol{\nabla} Y_v)}{\rho_g} & \text{(1d)} \end{cases}$$

where $\frac{D[\cdot]}{Dt} = \frac{\partial[\cdot]}{\partial t} + \boldsymbol{u} \cdot \nabla[\cdot]$ is the material derivative operator. ρ, $\boldsymbol{u}$, and P are the density, velocity, and pressure, respectively. $\bar{\bar{\Omega}} = -P\bar{\bar{I}} + \bar{\bar{\tau}}$ is the total stress tensor and $\bar{\bar{I}}$ the identity matrix. The viscous stress tensor is defined as:

$$\bar{\bar{\tau}} = 2\mu\bar{\bar{\Xi}} - \frac{2}{3}\mu\left(\boldsymbol{\nabla} \cdot \boldsymbol{u}\right)\bar{\bar{I}}$$

where $\bar{\bar{\Xi}} = \frac{1}{2}\left(\boldsymbol{\nabla u} + \boldsymbol{\nabla u}^T\right)$ and μ the dynamic viscosity. σ is the surface tension, H is the mean curvature, and the surface tension forces are considered based on the Dirac function (δ_Γ). The mean turbulent kinetic energy is maintained near a prescribed value by a forcing method similar to Duret et al. (2012). It consist in employing the volume forces ($\boldsymbol{f_{vol}}$) as a source term defined as

$$\boldsymbol{f_{vol}} = A\boldsymbol{u'}$$

where A is a forcing coefficient and $\boldsymbol{u'}$ represent the velocity fluctuations.

T is the temperature, and Y_v is the vapor mass fraction, only defined in the gas phase because the liquid is considered a monocomponent fluid. Thermophysical properties, such as the thermal conductivity (λ), thermal dilatation coefficient (α_T), liquid heat capacities (c_{pl}), and mass diffusivity (D_m) are considered constants. However, the gas heat capacity (c_{pg}) is an averaged weighted by the vapor and air mass fractions:

$$c_{pg} = \sum_{k=a,v} Y_k c_{pk}$$

Since both phases are considered compressible, equations of state for each phase are needed to close the system 1. For the liquid, a modified version of Tait's equation is chosen:

$$\rho_l = \rho_0 \left(\frac{P - P_0}{B} + 1\right)^{\frac{1}{\gamma_l}} \tag{2}$$

where ρ_0 is a density at a reference state, P_0 is a reference pressure, B is a constant, which depends on the isothermal compressibility of the fluid, and γ_l is a parameter inherent to the fluid. In the gas phase, the ideal gas equation is used:

$$\rho_g = \frac{PM_g}{RT} \tag{3}$$

where R is the ideal gas constant and the gas molar mass (M_g) defined as:

$$M_g = \left[\sum_{k=a,v} \frac{Y_k}{M_k}\right]^{-1}$$

.

Similar to Caltagirone et al. (2011); Fuster and Popinet (2018); Duret et al. (2018), the following equation is implemented for the spatial and temporal evolution of the pressure:

$$\frac{\mathrm{D}P}{\mathrm{D}t} = -\rho c^2 \boldsymbol{\nabla} \cdot \boldsymbol{u} + \frac{\alpha_T c^2}{c_p} \left(\boldsymbol{\nabla} \cdot (\lambda \boldsymbol{\nabla} T)\right) \tag{4}$$

where c is the speed of sound. More detail about de development of eq. 4 can be found in Germes Martinez (2022). To consider the phase change in our system, proper jump conditions at the interface are included, ensuring the conservation of mass, momentum, and species in the whole domain. The additional jump conditions due to phase change are (Ishii and Hibiki, 2010; Martinez et al., 2021):

$$[\boldsymbol{u}] = \dot{\omega} \left[\frac{1}{\rho}\right]_\Gamma \tag{5}$$

$$\left[P - \boldsymbol{n} \cdot \left(2\mu \bar{\bar{\Xi}}\right) \cdot \boldsymbol{n}\right]_\Gamma = \sigma H - \dot{\omega}^2 \left[\frac{1}{\rho}\right]_\Gamma \tag{6}$$

$$[\lambda \nabla T]_\Gamma = -\dot{\omega}\ h_{lv} \tag{7}$$

$$\rho_g D_m \boldsymbol{\nabla} Y_v \cdot \boldsymbol{n}\big|_g^\Gamma = \dot{\omega}(1 - Y_{vs}) \tag{8}$$

where $[A]_\Gamma = A_l - A_g$ for a given variable A, $\dot{\omega}$ is the vaporization rate and h_{lv} the latent heat.

3. Numerical methods

In this work, an interface capturing method is coupled with a projection method to solve the system 1. A detailed explanation of the numerical methodology can be found in Martinez et al. (2021). This section presents a general overview of the main numerical methods used for our simulations.

3.1. Interface representation and projection method

The coupled level-set/volume of the fluid (CLSVOF) method for the interface representation proposed by Ménard et al. (2007) was modified to handle compressible fluids and phase change in the ARCHER code. To this end, two additional terms are added to the RHS of the liquid volume fraction (α_l) transport equation (see Duret et al. (2018) or Martinez et al. (2021) for more details about the derivation) :

$$\frac{\partial \alpha_l}{\partial t} + \boldsymbol{\nabla} \cdot (\alpha_l \boldsymbol{u}_l) = -\frac{\alpha_l}{\rho_l}\frac{D\rho_l}{Dt} - \frac{\dot{m}}{\rho_l} \tag{9}$$

where $\boldsymbol{u}_l$ is the liquid velocity and $\dot{m} = \rho_l \Sigma \|\boldsymbol{s_d}\|$ is the volumetric evaporation rate. $\dot{m}$ is estimated using the local surface density $\left(\Sigma = \frac{S_\Gamma}{V_{cell}}\right)$ where S_Γ is the local surface area computed after the PLIC reconstruction and V_{cell} is the volume of the grid cell. Additionally, the level set function (ϕ) is used to compute the geometrical properties of the interface, such as, the normals $\left(\boldsymbol{n} = \frac{\boldsymbol{\nabla}\phi}{|\boldsymbol{\nabla}\phi|}\right)$ and the curvature ($\kappa = -\boldsymbol{\nabla} \cdot \boldsymbol{n}$).

This work uses the projection method based on two velocities presented in Martinez et al. (2021) to consider compressibility effects and phase change. An Eulerian staggered grid is considered, where the velocities are defined on the faces and the scalars (e.g., P, α_l, T, Y_v) are located in the center of the cell. The two velocity fields obtained with this method are the liquid velocity field and its extension in the gas phase and the gas velocity field and its extension in the liquid phase, which are continuous at the interface. Then, a Ghost Fluid method (Fedkiw et al., 1999) is applied to consider the velocity jump at the interface and couple the two velocity fields.

3.2. Temperature and vapor mass fraction transport

The temporal evolution of the temperature field is obtained by solving eq. 1c. Here, a 5th-order WENO scheme is implemented to discretize the convective term, and a 2nd-order central difference scheme is used for the diffusion term. Moreover, the energy jump condition at the interface is handled using a Ghost Fluid method. To avoid numerical heating/cooling during the solution of the convective term of eq. 1c or the interface transport, the temperature at each phase is extrapolated linearly using Aslam's extension method (Aslam (2004)).

Concerning the vapor mass fraction, eq. 1d is solved in the gas phase. The diffusive and convective term of eq. 1d are discretized using the same numerical schemes used for the temperature. At the interface, a Dirichlet boundary condition is implemented using the Aslam-Chiu extension method described in Bouali et al. (2016). To compute the vapor mass fraction at the interface (Y_{vs}), thermodynamic equilibrium is assumed. The saturation pressure (P_{sat}) is computed using the Clausius-Clapeyron relation:

$$P_{sat} = P_{ref} \exp\left[-\frac{h_{lv} M_v}{R}\left(\frac{1}{T^{\Gamma}} - \frac{1}{T_{ref}}\right)\right] \tag{10}$$

where P_{ref} is the saturation pressure at T_{ref}, M_v is the molar mass of the vapor and T^{Γ} is the interface temperature. Then, Y_{vs} is estimated with the following relation:

$$Y_{vs} = \frac{X M_v}{X M_v + (1 - X) M_a} \tag{11}$$

where $X = \frac{P_{sat}}{\overline{P}}$ is the vapor molar fraction and $\overline{P}$ is the mean pressure of the system.

Finally, the evaporation rate is computed from eq. 8, using the normal gradient of the vapor mass fraction at the interface:

$$\dot{\omega} = \frac{\rho_g D_m \boldsymbol{\nabla} Y_v \cdot \boldsymbol{n}|_g^{\Gamma}}{(1 - Y_{vs})} \tag{12}$$

3.3. Surface averaged quantities

The following sections investigate surface averaged variables to describe the vaporization process. The numerical methodology used to obtain such quantities is detailed in this section.

First, the interface is reconstructed by discretizing the zero level-set surface with a triangulated mesh using a Marching Cube algorithm. Then, its geometrical properties, such as surface area and mean curvature, are extracted. To this end, we use the "$surface\_operators$" routines of the in-house PyArcher code for post-processing. These routines are based on earlier versions of the routines described by Mohamed et al. (2019) and Di Battista et al. (2019) available through the project Mercur(v)e [1].

Then, interpolation schemes of order 0 and 1 are implemented to estimate the evaporation rate and vapor mass fraction at the zero level-set surface, respectively. Finally, the surface averaged quantities are calculated as follows:

$$\overline{\psi}^{\Gamma} = \frac{1}{S_r} \int \psi dS_r \tag{13}$$

where ψ is a scalar (here $\dot{\omega}$ or Y_v), dS_r is the local surface in a given cell and S_r is the total surface area reconstructed from the zero level-set surface.

4. Numerical configuration

The well-known two-phase homogeneous isotropic turbulence (Duret et al. (2012); Duret (2013); Duret et al. (2018)) is retained to study mixing and vaporization. However, heat and mass transfer was not considered in previous works. Here, the fluid thermophysical properties, initial temperature of each phase, and vapor concentration in the box must be specified carefully: they will dictate the vaporization regime observed until a saturation state is reached.

Consequently, the following section aims to estimate the equilibrium state that should be reached with a given set of physical parameters and initial temperatures. Based on this equilibrium, two different regimes of vaporization and mixing are chosen and investigated. The equilibrium is deduced from an iterative algorithm based on the first law of thermodynamics.

4.1. Equilibrium Conditions

Phase equilibrium is achieved when there is no mass transfer between the phases (Cengel et al., 2011). In other terms, the system has reached phase equilibrium when there is no vapor mass fraction gradient, which is the driving

---

[1] http://docs.mercurve.rdb.is/

force for mass transfer. Since the vapor mass fraction at the interface is a function of the temperature, thermal equilibrium is implied when the system reaches phase equilibrium. Therefore, in this work, the word equilibrium refers to phase equilibrium.

An energy balance is performed to estimate the system's conditions at the equilibrium state. By considering a closed system where three components (air, vapor, and liquid) coexist at the same time, we can write:

$$\Delta U_l + \Delta U_a + \Delta U_v = 0 \tag{14}$$

where

$$\Delta U_l = m_{l,eq} c_{vl} T_{eq} - m_l^0 c_{vl} T_l^0 - \left(m_{l,eq} - m_l^0\right) h_{lv}$$

$$\Delta U_a = m_{a,eq} c_{va} T_{eq} - m_a^0 c_{va} T_a^0$$

$$\Delta U_v = m_{v,eq} c_{vv} T_{eq} - m_v^0 c_{vv} T_v^0$$

represent the internal energy change between the initial and the final state of the liquid, air, and vapor phase, respectively. Here, m_i^0, $m_{i,eq}$ and T_i^0 are the initial mass, the mass at the equilibrium and the initial temperature of the component $i = l, a, v$. An expression for the equilibrium temperature (T_{eq}) is determined from eq. 14, considering the following assumptions:

- Heat capacities of each component are constant.
- Air is not soluble in the liquid.
- Initial temperature of the air and vapor are the same.
- There is no chemical reaction.

$$T_{eq} = \frac{m_l^0 c_{pl} T_l^0 + m_a^0 c_{pa} T_a^0 + m_v^0 c_{p,v} T_g^0 - m_{evap} h_{lv}}{m_{l,eq} c_{pl} + m_a^0 c_{pa} + m_{v,eq} c_{pv}} \tag{15}$$

The amount of evaporated mass can be determined by $m_{evap} = m_{v,eq} - m_v^0$. An iterative algorithm is used to solve eq. 15 with the condition that the vapor mass fraction calculated with the equilibrium temperature is the same as the vapor mass fraction calculated with the equilibrium vapor mass.

4.2. Parameters choice

Similar to previous works (Duret et al. (2018); Martinez et al. (2021)), a compressible two-phase HIT configuration with phase change is considered to study the scalar turbulent mixing and evaporation. Simulations are carried out in a 3D periodic box with a length size $l_x = 1.5 \times 10^{-4}\,m$, a liquid volume fraction $\alpha_l = 10\%$ and a mesh of 256^3. The mean turbulent kinetic energy is $\overline{k} = 3.6\; m^2 \cdot s^{-2}$, the liquid has the physical properties of n-decane, and the gas is initially considered dry air. Additionally, once evaporation starts, the gas phase is considered an ideal mixture of air and n-decane vapor. The physical properties at the initial state of the simulation are summarized in the table 1. The parameters for the Tait's equation are $B = 10^9\,Pa$, $P_0 = 10^5\,Pa$, $\rho_0 = 750\,kg{\cdot}m^{-3}$ and $\gamma_l = 1.215$. Moreover, the initial values of the simulation's dimensionless numbers are listed in table 2.

Fluid	$\rho\left(\frac{kg}{m^3}\right)$	$\mu\left(\frac{kg}{ms}\right)$	$\lambda\left(\frac{W}{mK}\right)$	$C_p\left(\frac{J}{kgK}\right)$	$M\left(\frac{kg}{mol}\right)$	$h_{lv}\left(\frac{J}{kg}\right)$
Air	25	1.88×10^{-5}	0.045	1060	0.029	-
Vapor	-	-	-	2098	0.142	-
N-decane	750	5.65×10^{-4}	0.14	2207	0.142	3.25×10^5

Table 1: Physical properties for the air, vapor, and n-decane at the initial state of the simulation.

Fluid	Sc	Pr	Le
Air	1.96	0.44	4.44
N-decane	-	8.90	-

Table 2: Dimensionless numbers at the initial state of the simulations.

Two simulations are performed to investigate the influence of the evaporation regime on scalar turbulent mixing, where only the initial liquid temperature is varied. The initial liquid temperatures of the simulations are $T_l^0 = 540\,K, 460\,K$ and the initial gas temperature in both cases is $T_g^0 = 573\,K$. The first simulation is expected to present a larger evaporation rate than the second since the liquid temperature is closer to the boiling point. Hence, the equilibrium state and the temporal evolution of the temperature and vapor mass fraction are expected to differ in both simulations.

Cases	$T_l^0(K)$	$T_g^0(K)$	$T_{eq}(K)$	$Y_{v,eq}$	$\frac{m_{l,eq}}{m_l^0}$	$\frac{P_{eq}}{P_0}$
1	540	573	522	0.44	0.76	1.03
2	460	573	464	0.19	0.93	0.83

Table 3: Different variables at the equilibrium state for the two cases studied.

Using the method presented in section 4.1, the variables at the equilibrium are estimated for each case, and the results are summarized in the table 3. In the hypothetical case where evaporation is not considered in the system (only heating), the equilibrium temperature is between the initial liquid and gas temperatures. The table 3 shows that the equilibrium temperature for case 1 is lower than the initial liquid temperature. This is explained by the large evaporation rate, where the liquid's latent heat consumes an important part of the initial energy of the system. In contrast, different results are observed for case 2, where the equilibrium temperature is higher than the initial liquid temperature. Since case 2 has a lower evaporation rate, the system's energy in the initial state is sufficient to evaporate the liquid and increase its temperature. However, the increase in liquid temperature is lower than in the hypothetical case without evaporation because some energy is still consumed. In both cases, the equilibrium temperature is smaller than the gas temperature.

Moreover, the impact of the evaporation regime can be seen in the amount of liquid evaporated. In case 1, the equilibrium vapor mass fraction is 2.3 times larger compared to case 2. This indicates a more significant amount of evaporated liquid in case 1, caused by the increased evaporation rate. Another parameter is the liquid mass at equilibrium normalized by its initial value. Again, a lower liquid mass is observed for case 1, which agrees with the aforementioned discussion.

The variables at the equilibrium are used to normalize the temperature

($T^* = \frac{T}{T_{eq}}$) and the vapor mass fraction ($Y_v^* = \frac{Y_v}{Y_{v,eq}}$). In addition, to analyze different stages of the turbulent mixing, four times are defined (t_1, t_2, t_3 and t_4), each corresponding to a time where a specific value of the normalized mean vapor mass fraction is reached ($\overline{Y_v}^* = 0.18, 0.32, 0.54$ and 0.72). It is important to note that the physical time represented by each defined time varies depending on the simulation. For example, since the vapor production rate is higher in case 1, t_1 represents a shorter time compared to case 2. Furthermore, the values of $\overline{Y_v}^*$ were chosen considering the time required to reach the equilibrium state and the computational cost involved. Nevertheless, at least 20 eddy turnover times are considered for each simulation to have a well-developed mixture of the vapor mass fraction.

4.3. Initialization procedure

The simulation initialization is similar to Duret et al. (2012); Bouali et al. (2016) for the velocity fields. Regarding heat and mass transfer, the temperature is constant in each phase during the initialization procedure, meaning that no diffusion of species or heat occurs during this stage. Then, sub-iterations of pure diffusion are performed, where the following equations are solved:

$$T^{k+1} = T^k + \frac{\Delta t_{diff}}{\rho^k c_p^k} \boldsymbol{\nabla} \cdot \left(\lambda \boldsymbol{\nabla} T^k \right) \tag{16a}$$

$$Y_v^{k+1} = Y_v^k + \Delta t_{diff} \frac{\boldsymbol{\nabla} \cdot \left(\rho_g^k D_m \boldsymbol{\nabla} Y_v^k \right)}{\rho_g^k} \tag{16b}$$

where k is the current sub-iteration. The number of diffusive sub-iterations (k_{end}) is computed by:

$$k_{end} = \frac{t_{BL}}{\Delta t_{diff}} \tag{17}$$

where $t_{BL} = \frac{\delta_{Yv}}{s_{diff}}$ is the time to generate a vapor boundary layer close to the interface. More precisely, this procedure move a vapor mass fraction iso-contour to an imposed distance $\delta_{Y_v} = 6dx$ with an estimated speed of $s_{diff} = \frac{D_m}{dx}$. $\Delta t_{diff} = \frac{0.2}{V_{cfl}}$ is the time step computed with the thermal and mass diffusion restrictions:

$$D_{cfl} = \frac{6Diff}{dx^2}$$

where $Diff = \max\left(\frac{\lambda_g}{\rho_g c_{pg}}, \frac{\lambda_l}{\rho_l c_{pl}}, D_m\right)$.

This procedure avoids numerical instabilities in the vaporization rate computation created by high temperature and vapor mass fraction gradients in the initial fields. Finally, the energy and vapor mass fraction transport equations are activated, and the simulation statistics are taken from this point.

5. Results

5.1. Heat and mass transfer

The instantaneous temperature fields at the domain boundaries with interface visualization (zero level set isocontour) at t_3 for each case are presented in Figure 1 (top). At this point in the simulations, the effects of the turbulent velocity field are easily appreciated in the temperature transport. The interface visualization opacity is reduced to show the bubbles enclosed within the larger liquid structures. Due to the reduced gas volume, these bubbles are characterized by a higher saturation level than the gas far from the interface. The influence of the gas volume on time required to reach equilibrium is investigated in more detail by Duret et al. (2012).

Additionally, a wide range of vapor mass fraction gradients is observed near the interface. These variations depend mainly on the interface's deformation and the surrounding gas's temperature. For example, a liquid structure moving toward a high-temperature gas will exhibit a smaller thermal boundary layer thickness at the front due to the larger temperature gradients.

Similar phenomena are observed in Figure 1 (bottom) for the instantaneous vapor mass fraction fields at the domain boundaries at t_3. Compared to the temperature fields, larger gradients are present in the gas phase: convection effects are more dominant for this scalar because the mass diffusivity ($D_m = 3.82 \times 10^{-7}\, m^2 \cdot s^{-1}$) is smaller than the initial thermal diffusivity ($D^{th} = 1.70 \times 10^{-6}\, m^2 \cdot s^{-1}$).

Figure 2 shows the volume rendering of the vapor mass fraction at the same time as Figure 1. Here, we can observe the interactions of the vapor mass

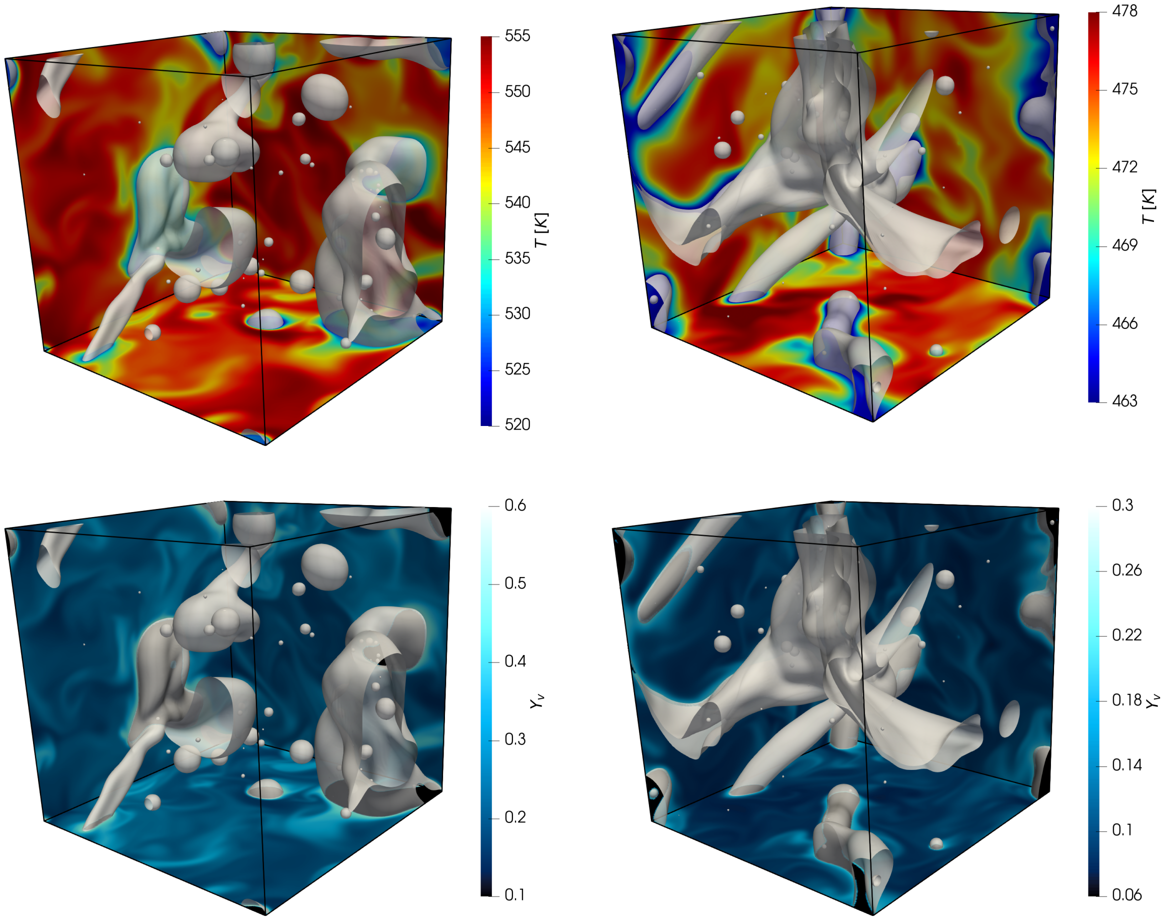

Figure 1: Instantaneous temperature (top) and vapor mass fraction (bottom) fields at the domain boundaries with interface visualization (zero level set isocontour) at t_3 for case 1 (left) and case 2 (right).

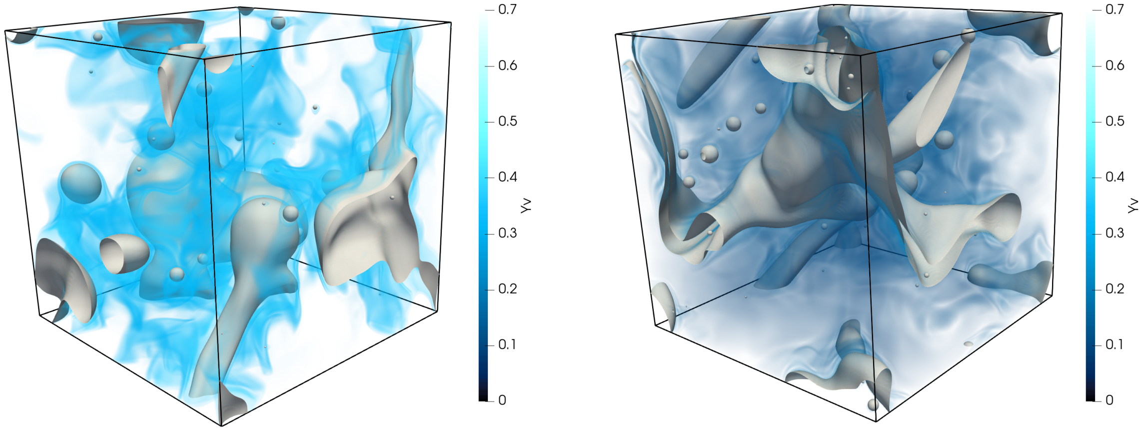

Figure 2: Volume rendering of the vapor mass fraction field with interface visualization (Level Set 0 isocontour) at t_3 for the two cases studied.

fraction and the turbulent velocity field within the domain. There is vapor accumulation near the interface region, and the vapor begins to saturate the entire gas volume until the system reaches equilibrium. Another interesting phenomenon is the vapor wake behind the smaller liquid structures as they are convected through the domain. There are several possible outcomes for the lifetime of these smaller liquid structures, e.g., they may remain convected by the velocity field until their complete evaporation, or they could merge with another liquid structure. These possible scenarios are considering that the system is not at equilibrium. Furthermore, it is noted that the size and shape of vapor wakes depend on the size of the structure, its average velocity, and the distance from another interface.

Recently, similar observations have been made for a single evaporating droplet in a homogeneous and isotropic turbulent environment (Dodd et al. (2021)) and for dispersed evaporating droplets in a homogeneous turbulent shear environment (Scapin et al. (2021)). In Scapin et al. (2021), the authors show variations in the evaporation rate due to small deformations caused by the turbulent velocity field. In addition, their results also reveal an increase in the evaporation rate due to the interaction of the vapor mass fraction with the turbulent velocity field. These results highlight the limitation of classical vaporization models based on spherical droplets with a constant evaporation rate.

The temporal evolution of the liquid and interface temperature normalized by the equilibrium temperature for both cases are presented in Figures 3. $t^* = \frac{t}{\tau}$ is the time normalized by the eddy turnover time defined as:

$$\tau = \frac{\overline{k}}{\overline{\epsilon}}$$

where $\overline{(\cdot)}$ is the volume averaging operator, and $\overline{\epsilon}$ is the mean turbulent dissipation rate. As predicted, the temperature of the liquid for case 1 decreases as it approaches the equilibrium state (see Figure 3a). In addition, the liquid temperature follows the temperature at the interface, decreasing despite the higher gas temperature because of the heat jump caused by the latent heat. This result shows the accuracy of the Ghost Fluid Method implemented to account for the energy jump condition and the coupling between the liquid and gas temperature. At the first instants of the simulation, a sudden drop in temperature is observed before it starts to stabilize after two eddy turnover times. It can be explained by the maximum value of the evaporation rate during the early moments of the simulation. Subsequently, the vapor generated accumulates at the interface, decreasing the evaporation rate and slowing the temperature decrease. At the end of the simulation, there is a negative slope in the evolution of the liquid temperature, which means that heat is still exchanged with the gas phase, i. e., equilibrium has not yet been reached.

An opposite behavior is observed for the liquid temperature in case 2. Figure 3b shows an increase in the liquid temperature caused by the initial temperature gradient between the liquid and gas. Then, the temperature rise slows down as the heat flux from the gas to the liquid and the evaporation rate decrease. Consequently, the behavior of both cases is the same as the one predicted by the iterative algorithm described in section 4.1.

The temporal evolution of liquid and interface temperature is strongly linked to the evaporation rate due to the energy jump condition at the interface. Thus, the temporal evolution of the surface-averaged evaporation rate $\left(\overline{\dot{\omega}}^{\Gamma}\right)$ for both

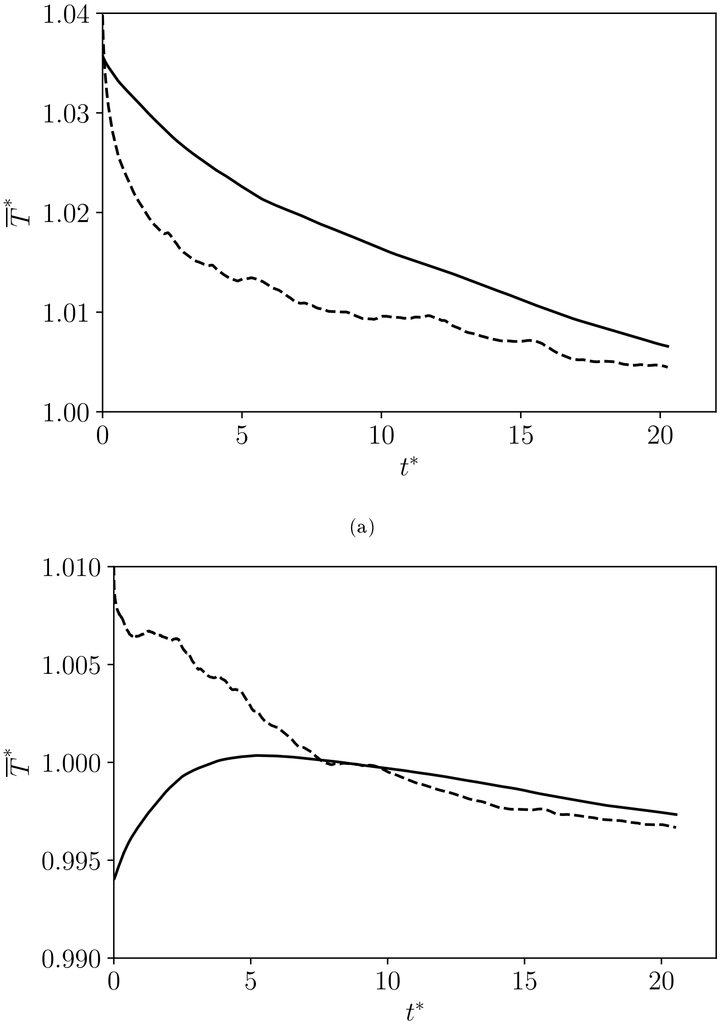

(a)

(b)

Figure 3: Normalized liquid (solid line) and interface (dashed line) temperatures temporal evolution for case 1 (a) and case 2 (b).

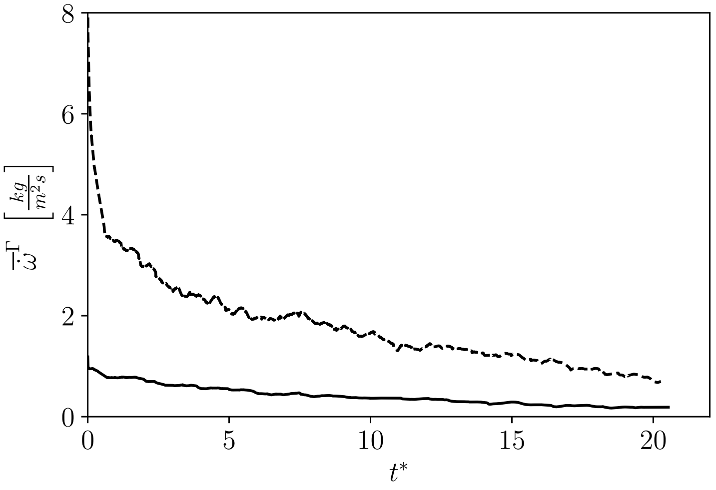

Figure 4: Evaporation rate temporal evolution for case 1 (dashed line) and case 2 (solid line).

cases is shown in Figure 4. By comparing each case, a significant difference between the initial magnitudes of $\overline{\dot{\omega}}^{\Gamma}$ is observed, which is explained by the initial liquid temperatures chosen for each case. Nevertheless, both curves have the same general behavior; a maximum value at the beginning of the simulation followed by a decrease as the system approaches equilibrium.

The temporal evolution of the normalized volume-averaged gas temperature ($\overline{T}_g^* = \frac{\overline{T}_g}{T_{eq}}$) is shown in Figure 5. Here, a more pronounced temperature decrease is observed in case 2 compared to case 1. The effect of the energy jump and the Stefan flow on the heat transfer across the interface could explain this behavior. In case 1, the temperature decrease near the interface caused by latent heat results in an important local decrease in the temperature gradient. In other words, the increased evaporation rate slows down the heat transfer. The decrease in the heat transfer due to the Stefan flow has also been observed in the literature by Jayawickrama et al. (2019, 2021) in vaporizing droplet configurations.

Another way to investigate the influence of the evaporation rate on the evolution of a system from the initial condition to the equilibrium state is to study the temporal evolution of $\overline{Y}_v^*$ shown in Figure 6 for the two cases studied.

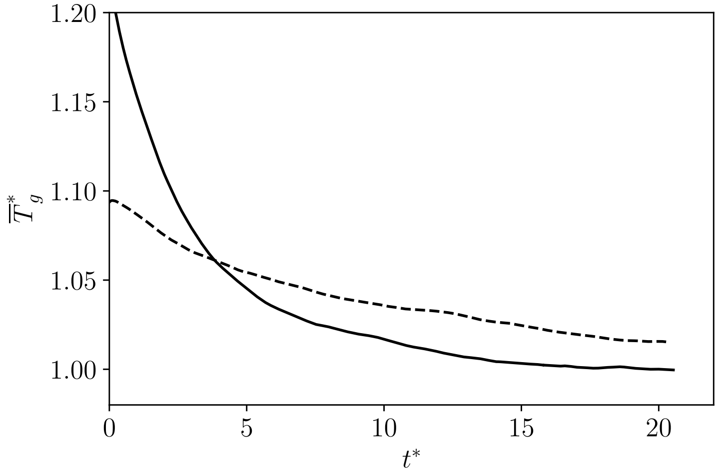

Figure 5: Normalized gas temperature temporal evolution for case 1 (dashed line) and case 2 (solid line).

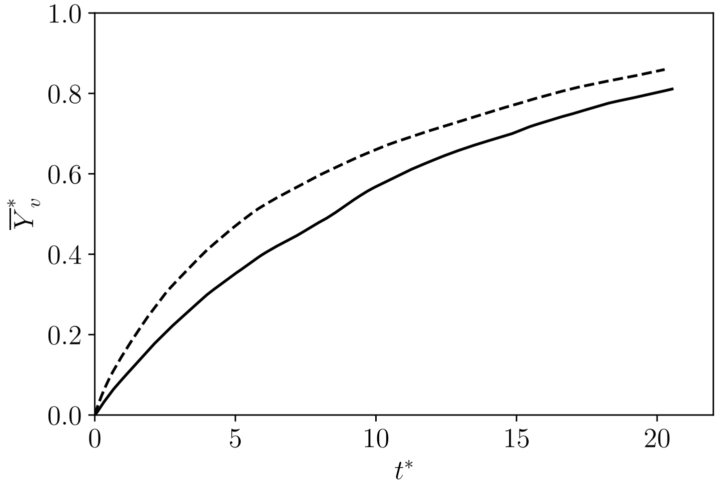

Figure 6: Normalized vapor mass fraction temporal evolution for case 1 (dashed line) and case 2 (solid line).

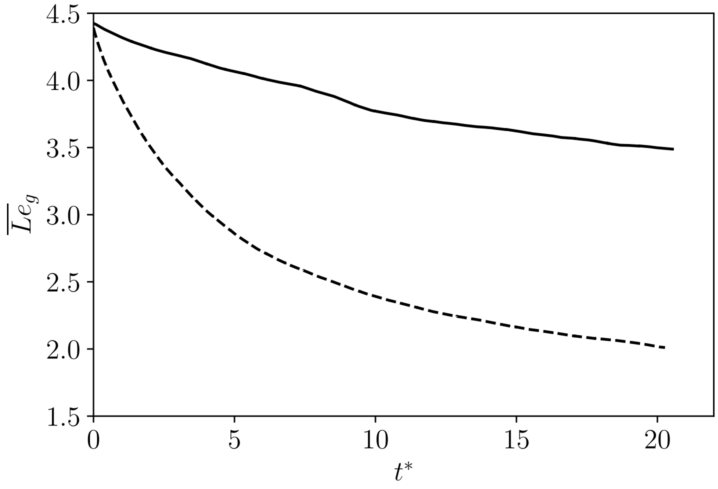

Figure 7: Gas Lewis number temporal evolution for case 1 (dashed line) and case 2 (solid line).

Here, we can observe a more rapid increase of $\overline{Y}_v^*$ in case 1. These results are consistent with our previous analysis of the temporal evolution of the mean liquid and gas temperatures and evaporation rate: higher evaporation rates indicate faster vapor generation at the interface, contributing to the increase of $\overline{Y}_v^*$ in case 1. In addition, the increased Stefan flow pushes the vapor away from the interface, contributing to vapor mixing. However, the time evolution of $\overline{Y}_v^*$ depends not only on the conditions near the interface (T^Γ, $\bar{\dot{\omega}}^\Gamma$, etc.), but it also depends on the turbulent velocity field and the interaction between the liquid and gas structures. This last part is investigated in the following sections by analyzing the evolution of the second moment and the PDFs of $\overline{Y}_v^*$.

From Figures 5 and 6, we can notice different characteristic times needed to reach the thermal equilibrium ($\overline{T}_l^* = \overline{T}_g^* = 1$) and the phase equilibrium ($\overline{Y}_v^* = 1$) in both cases. This can be explained by looking the evolution of the gaseous Lewis number $\left(\overline{Le}_g = \frac{\overline{D^{th}}}{D_m}\right)$ shown in Figure 7. Both cases have an initial $\overline{Le} = 4.44$, indicating a stronger thermal diffusion influence, resulting in a reduction of the characteristic time to reach the thermal equilibrium. However, the Lewis number is not constant in our simulations due to the decrease of the

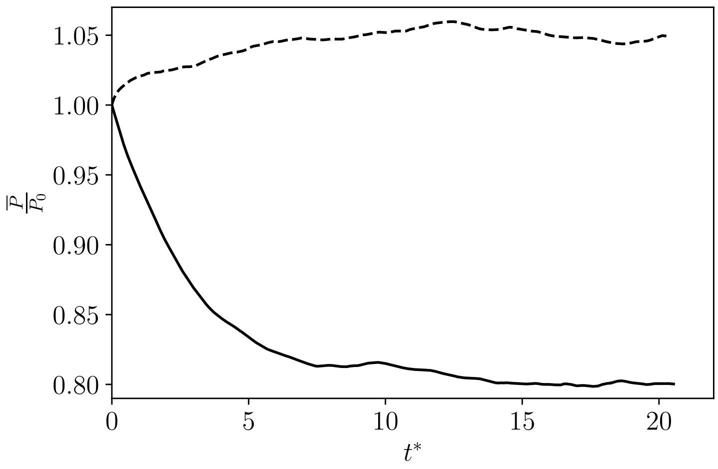

Figure 8: Normalized pressure temporal evolution for case 1 (dashed line) and case 2 (solid line).

gaseous thermal diffusion coefficient $\left(\overline{D_g^{th}} = \frac{\lambda_g}{\rho_g c_g}\right)$ induced by the increase of the gas density and heat capacity. Consequently, the evaporation regime influences the difference between the thermal and mass characteristic times. For example, these times will tend to approach each other more rapidly in case 1 due to the faster increase of the mean vapor mass fraction. These results show that large evaporation rates induce a relatively high Lewis number variation, limiting the assumption that the Lewis number is constant and equal to one, normally used in turbulent combustion mixing models.

The temporal evolution of the normalized mean pressure $\left(\overline{P}^* = \frac{\overline{P}}{P_{eq}}\right)$ for each case is shown in Figure 8. The pressure variations in both cases can be explained by analyzing the time evolution of temperature and vapor mass fraction. In our simulations, the vapor molecular mass is greater than the air molecular mass, increasing the mean molecular mass of the gas phase, which will tend to increase the system pressure as the liquid evaporates. In contrast, the decrease in gas temperature in both cases will tend to decrease the system pressure. In case 1, a slight increase in initial pressure is observed, resulting from the amount of vapor produced, which compensates for the pressure drop due to the decrease in temperature. However, as less liquid evaporates in case 2, the pressure experiences a significant decrease. These results agree well with the behavior predicted by the algorithm presented in the section 4.1, summarized in the table 3.

5.2. Scalar turbulent mixing analysis

5.2.1. Evolution of the scalar variance

This section studies scalar mixing using the normalized vapor mass fraction second moment. This has been previously done for single-phase (Eswaran and Pope (1988); Juneja and Pope (1996)), dispersed (Reveillon et al. (1998); Reveillon and Vervisch (2000); Reveillon and Demoulin (2007)) and dense (Duret et al. (2012)) two-phase flows. In the first scenario, several power laws for the scalar variance decay can be found in the literature, depending on whether an imposed mean scalar gradient feeds the scalar. This behavior is explained by the dissipation rate term in the variance transport equation. In the DNS of dispersed two-phase flows, Lagrangian techniques are implemented to track the temporal evolution of droplet diameter, velocity, and position. These droplets create vapor pockets as the turbulent velocity field convects them. This kind of simulation provides good insight into the effects of a non-homogeneous scalar source on the temporal evolution of the scalar variance. However, some limitations arise, for instance, the interactions between the scalar and the liquid/gas interface are not solved, and an idealized model for liquid vaporization is used.

In this work, the interface and internal flows of liquid structures are solved, similar to Duret et al. (2012). Moreover, our formalism coupled temperature, vapor mass fraction, and fluid dynamics through the evaporation rate. Consequently, the vapor mass fraction is not a passive scalar, and the mixing and the fluid dynamics of the system depend on the mass and thermal boundary layers simultaneously.

Figure 9 shows the temporal evolution of the RMS (Root Mean Square) of

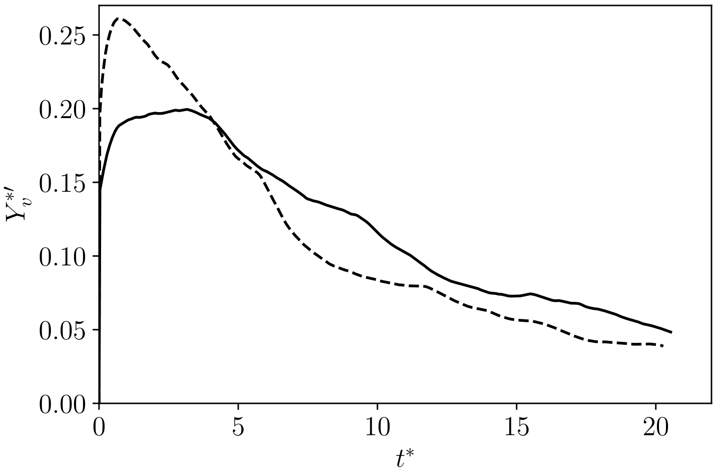

Figure 9: Temporal evolution of $Y_v^{*\prime}$ for case 1 (dash line) and case 2 (solid line).

the normalized vapor mass fraction, computed as follows:

$$\left(Y_v^{*\prime} = \sqrt{\overline{(Y_v^* - \overline{Y_v^*})^2}} \right)$$

for the two cases studied. The curves in Figure 9 have similar behavior. An increase in the RMS is observed at the beginning of the simulation. Then, it reaches a maximum value after approximately an eddy turnover time, before its decay towards zero. This behavior differs from the results obtained with the single-phase flow but is similar to those obtained with the two-phase dispersed flow simulations. As discussed by Reveillon and Vervisch (2000), the initial increase in scalar RMS is caused by the source terms appearing in its transport equation when an evaporating liquid generates vapor. The maximum value of the RMS is reached when the scalar dissipation rate balances the dispersion generation. After reaching the maximum, turbulent mixing becomes more influential in the system than vaporization, resulting in a decay of the scalar variance.

Moreover, Duret et al. (2012) observed similar behavior in dense two-phase flow simulations. In this case, the initial increase in dispersion is influenced by vapor generation at the interface and the diversity of boundary layer thickness formed around the liquid structures. Furthermore, the initial liquid volume fraction on the time evolution of the scalar variance is investigated. It is observed that a decrease in the available gas volume causes an increase in the maximum value of the scalar RMS and a sharper subsequent decay, resulting in a shorter saturation characteristic time.

In a more detailed analysis of the curves presented in Figure 9, we observe the evaporation regime's influence on the scalar variance's temporal evolution. For a higher evaporation rate, the maximum value of the variance increases and is reached in a slightly shorter time than in case 2. Moreover, the subsequent decay of the scalar dispersion is also more pronounced for the case with a large evaporation rate. A similar observation was made by Reveillon and Vervisch (2000) for dispersed two-phase flows. This is explained by the faster generation of vapor in the dry air environment and the subsequent mixing of this vapor. In this work, the scalar variance depends not only on the magnitude of the evaporation rate but also on the temporal evolution of the surface density, the influence of the Stefan flow on the system dynamics, and the curvature of the interface, resulting in a more realistic model of the atomization, mixing, and evaporation processes. For example, the Stefan flow pushes the vapor away from the interface, contributing to the decay of the scalar RMS and consequently enhancing the mixing process. In addition, the non-homogeneity of the evaporation rate considered in the present work dramatically affects the temporal and spatial evolution of the scalar dissipation rate and, consequently, the scalar variance.

The following sections perform a more detailed analysis of scalar generation and mixing by computing scalar PDFs and joint PDFs.

5.2.2. Evolution of the scalar PDFs

The asymptotic behavior of scalar mixing has been extensively studied and is well known in the literature. For a confined two-phase environment with a vaporizing liquid surrounded by dry air, the scalar PDF starts as a shape similar to a Dirac function where $\overline{Y}_v^* = 0$ if evaporation has not started yet. Then, vaporization occurs and when the equilibrium state is finally reached, the scalar PDF has a similar shape at $\overline{Y}_v^* = 1$, where vapor generation is no longer possible due to the absence of a vapor gradient.

In this work, we are interested in studying the temporal evolution of scalar PDF shapes. For this purpose, the PDF of the normalized vapor mass fraction for four successive instants for case 1 is plotted in Figure 10. The general tendency described above is easily seen. An interesting behavior that is observed for the curves presented in Figure 10a is the presence of values of $\overline{Y}_v^* > 1$. Hence, the vapor mass fraction is not upper-bounded to 1 when normalized by its saturation state value, even though it is its final value. This behavior has at least two explanations; first, from the table 3, we can observe that the temperature at equilibrium is lower than the liquid temperature. Consequently, the equilibrium interface vapor mass fraction is smaller than the initial vapor mass fraction.

Secondly, there is a wide range of liquid structures with different characteristic lengths, resulting in different temporal evolution of temperature profiles in each liquid structure. This means that some smaller liquid structures do not have the same behavior as the overall system. For example, a small convected droplet in contact with high-temperature gas will evaporate and increase in temperature simultaneously, even though the system's average temperature tends to decrease. This is also a consequence of solving the temperature and internal flow of the liquid structure. Furthermore, these results demonstrate the strong coupling between the energy and species conservation equations and the variety of phenomena captured by our compressible formalism.

In the analysis of passive scalar mixing in single-phase flows, values of the normalized vapor mass fraction greater than unity are generally not observed. In the literature, the total amount of vapor is usually imposed at the initial condition of the simulation. In the simulation performed by Duret et al. (2012), the vapor mass fraction at the interface is constant and imposed during simulation initialization. Consequently, the temporal evolution of the temperature and its relation with the vapor mass fraction is not solved. As a result, the equilibrium vapor mass fraction equals the imposed vapor mass fraction at the interface.

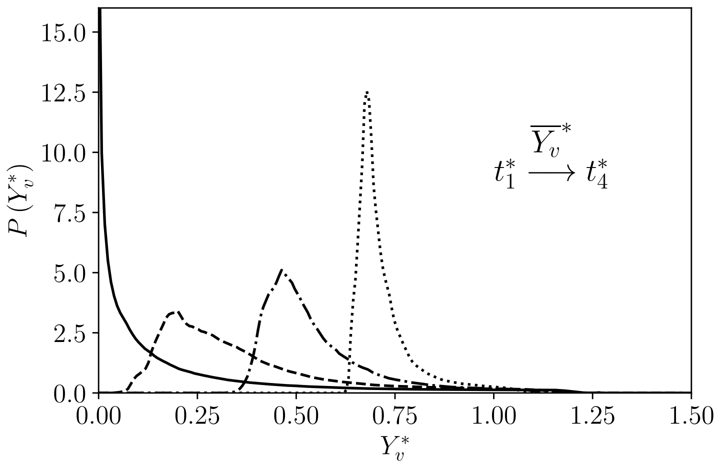

(a)

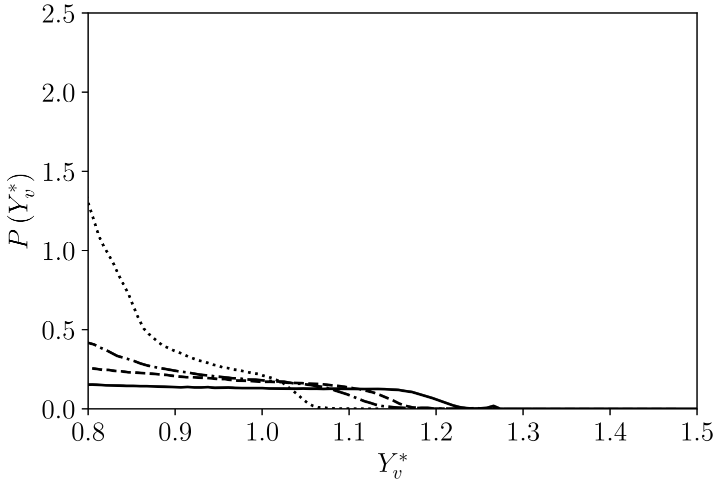

(b)

Figure 10: (a) Instantaneous PDFs of Y_v^* at t_1^* (solid line), t_2^* (dashed line), t_3^* (dashed-dotted line) and t_4^* (dotted line), and (b) Zoom of the higher values of Y_v^* at the same times for case 1.

The first PDF presented in Figure 10a correspond to a normalized time of $t_1^* = 0.94$. At this time, the RMS is almost at its maximum ($Y_v^{*\prime} = 0.26$). The PDF has a pronounced peak at $Y_v^{*\prime} = 0$ corresponding to dry air and a long tail containing all the possible values of the normalized vapor mass fraction. This corresponds to the first instants after the development of the mass boundary layer, where the mixing is mostly governed by diffusion of the vapor layers around the interface. This stage of the scalar mixing is characterized by large temperature and vapor mass fraction gradients at the interface, explaining the rate of change observed in the temporal evolution of the $\overline{T}_l^*$, $\overline{\dot{\omega}}^\Gamma$, $\overline{T}_g^*$, and $\overline{Y}_v^*$ (see Figures 3, 4, 5 and 6).

The following PDF corresponds to $t_2^* = 2.88$ and an RMS of $Y_v^{*\prime} = 0.22$, which means that the decay has already started; thus, the contribution of the scalar dissipation rate is more significant than the contribution of the vaporization source term in the variance transport equation. In this state, the effects of the turbulent velocity field on the scalar mixture are more critical. As a result, the vapor is transported into the gas field away from the interface, resulting in a rightward shift and a decrease in the PDF peak. In addition, the tail of the PDF has decreased, indicating a reduction in the vapor mass fraction at the interface.

Subsequently, at the third PDF, which corresponds to a time of $t_3^* = 6.21$, regrowth of the peak and a shrinking of the PDF are observed, showing a homogenization of the vapor mass fraction in the gas phase away from the interface, which is also characterized by a decay of the RMS ($Y_v^{*\prime} = 0.14$). In addition, the probability of values smaller than $\overline{Y}_v^* = 0.25$ is close to zero, which means that the vapor is spread over the entire gas volume. A tail is also present on the right side of the PDF, corresponding to the larger values close to the interface.

Finally, the shrinking continues in the fourth PDF: $Y_v^{*\prime} = 0.077$ at $t_4^* = 12.0$, which is consistent with the asymptotic behavior described above. The PDF peak is larger, and its shape has fewer irregularities, indicating a higher level of homogenization of the vapor mass fraction.

An interesting behavior is observed at the end of the right tails of the PDFs.

A zoom of the highest values of the Y_v^* is presented in Figure 10b. This way, the temporal evolution of the PDF tails is easily seen. Here, we see that the PDFs tails move to the left, towards unity. In addition, there is an abrupt behavior change in the last values of the PDFs. This could be interpreted as the result of the temporal evolution of the vapor mass fraction gradient near the interface. It is worth mentioning that these results describe a general behavior of the system and that the mass boundary layer thickness varies depending on the local thermodynamic conditions in each structure and each cell close to the interface.

The PDFs of the vapor mass fraction for the case 2 at the same level of mixing are presented in Figure 11. In this case, values of $\overline{Y}_v^* > 1$ can also be found but with a smaller probability than in case 1. Here, the equilibrium temperature is higher than the initial liquid temperature (see table 3). Consequently, a probable reason for having values of $\overline{Y}_v^* > 1$ is that the smallest liquid structures are heated at temperatures higher than the equilibrium temperature, which generates a high vapor mass fraction at the interface. This occurs especially in the first moments of the simulation. The probabilities for the values of $\overline{Y}_v^* > 1$ decrease with time until they become nonexistent in the last PDF.

Comparing the two studied cases, the influence of the evaporation rate in the PDF shapes can be observed. In case 2, the physical time needed to arrive at the same value of $\overline{Y}_v^*$ ($t_1^* = 1.79$) is almost 13 times higher than in case 1 due to the lower evaporation rate. As a consequence, the turbulent velocity field has more time to advect the vapor mass fraction field, resulting in a reduction of the PDF peak. Similar behavior is observed in the other PDFs. The second PDF correspond to a time of $t_2^* = 4.73$ and a $Y_v^{*\prime} = 0.137$. At this time, the peak of the PDF continues to decrease. In the third and fourth PDFs ($t_3^* = 8.99$ and $t_4^* = 15.26$), the width has been reduced considerably. This indicates that a more efficient turbulent mixing is achieved compared to case 1, but their behavior over time remains similar.

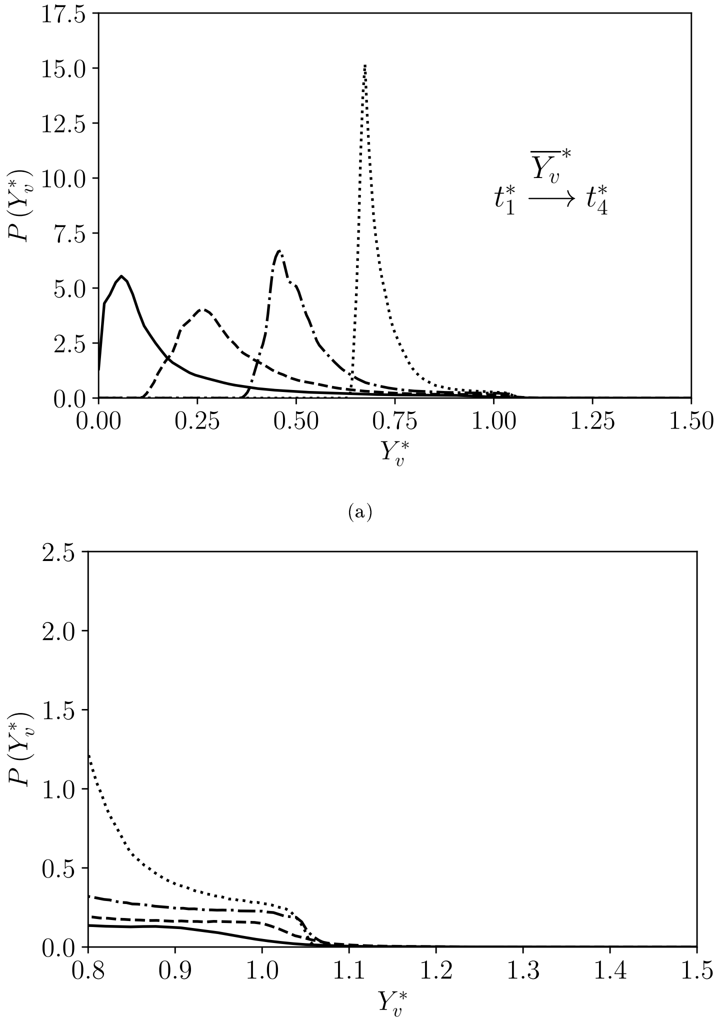

(a)

(b)

Figure 11: (a) Instantaneous PDFs of Y_v^* at t_1^* (solid line), t_2^* (dashed line), t_3^* (dashed-dotted line) and t_4^* (dotted line), and (b) Zoom of the higher values of Y_v^* at the same times for case 2.

5.2.3. Self-similarity

Figure 12 shows the normalized PDF of $\overline{Y}_v^*$ ($P(\overline{Y}_v^*)Y_v^{*\prime}$ with respect to $\frac{Y_v^*-\overline{Y}_v^*}{Y_v^{*\prime}}$). Similar to the results obtained by Duret et al. (2012), a significant asymmetry is observed in all the PDFs. The peaks are on the negative side of the x-axis, indicating that the smaller values far from the interface are dominant. In Figure 12a, the shape of the PDF is affected by the initial conditions in the early stages of the simulation. However, the PDF adopts similar shapes once the scalar mixing is more developed.

Nonetheless, around the peak, we can notice a difference in the shapes of the PDFs, especially in the low evaporation case. Compared with the results of the single-phase simulations, it is evident that the interface acting as a vapor source strongly influences the PDF shape. For example, the tail present on the right of all PDFs is the primary indicator of these differences.

The shape observed in Figure 12 is similar to the results obtained by Duret et al. (2012). However, there is a noticeable difference on the right-hand side of the PDFs. In the work of Duret et al. (2012), a secondary peak is formed at the maximum value of the scalar due to the interface boundary condition of the vapor mass fraction. In this work, the tail shape of the PDFs varies as a function of the vapor mass fraction at the interface, which is non-homogeneous and dependent of the interface temperature. Consequently, the vapor mass fraction at the interface possesses its own PDF, which will be investigated in the next section. In both cases, the shapes of the PDFs are similar to a log-normal distribution, confirming that the PDF shape is not adequately represented by a *beta* distribution when the interface acts as a scalar source.

5.2.4. Surface conditional PDFs

This section analyzes the temporal evolution of the evaporation rate and the vapor mass fraction at the interface. For this purpose, the PDFs for the same instants presented in the previous section are used.

Figure 13 shows the PDFs of the surface-averaged normalized vapor mass fraction $\left(Y_{vs}^* = \frac{Y_{vs}}{Y_{v,eq}}\right)$ at t_1^*, t_2^*, t_3^* and t_4^* for both cases. For the interface vari-

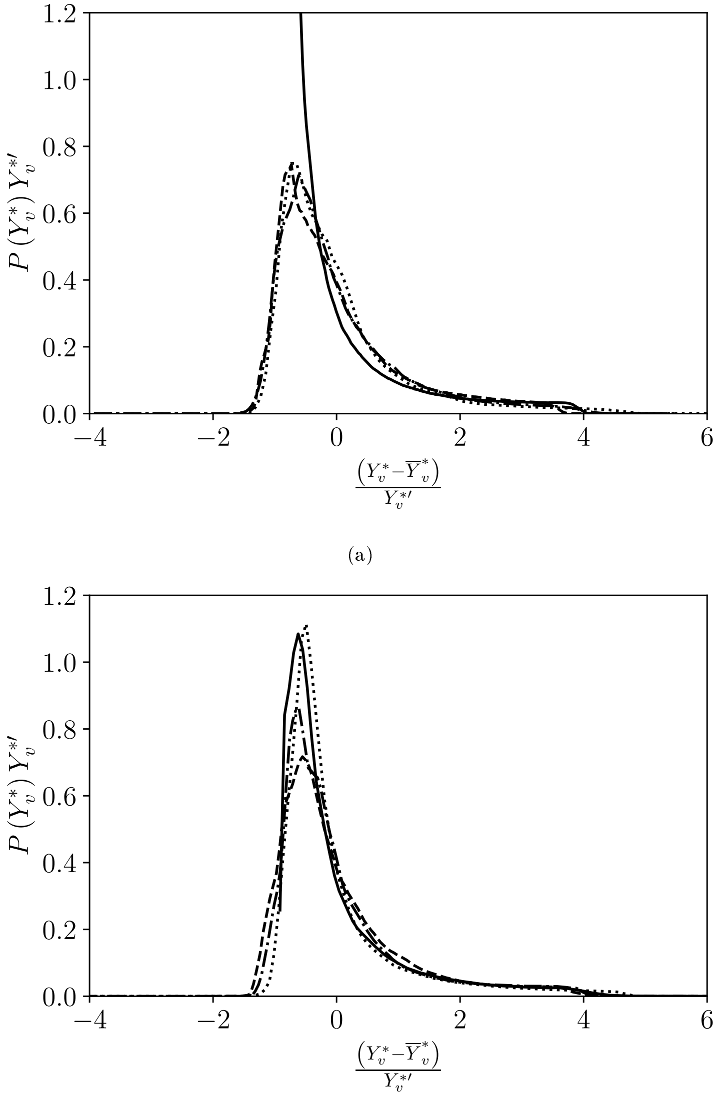

(a)

(b)

Figure 12: Instantaneous normalized PDFs of Y_v^* at t_1^* (solid line), t_2^* (dashed line), t_3^* (dashed-dotted line) and t_4^* (dotted line) for case 1 (a) and case 2 (b).

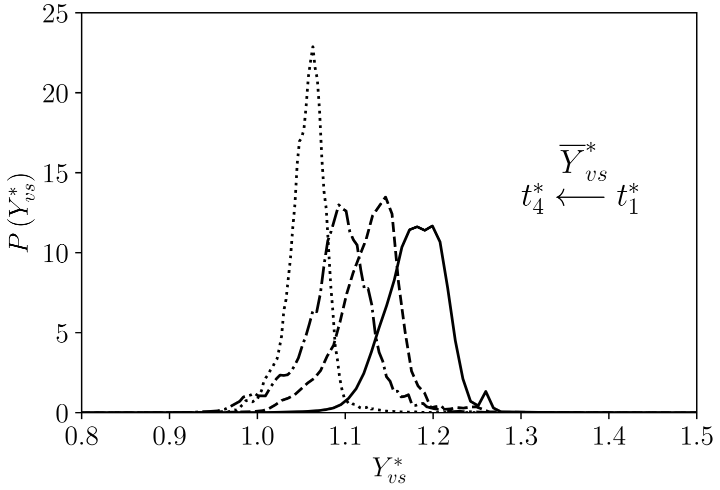

(a)

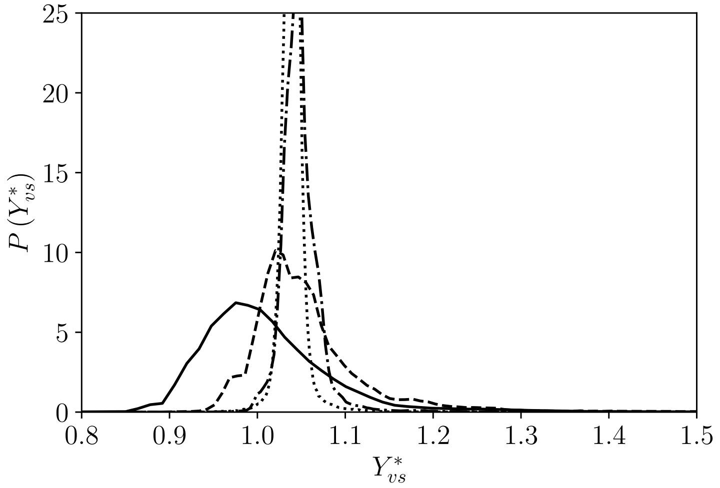

(b)

Figure 13: Instantaneous PDFs of Y^*_{vs} at t^*_1 (solid line), t^*_2 (dashed line), t^*_3 (dashed-dotted line) and t^*_4 (dotted line) for case 1 (a) and case 2 (b).

ables, the asymptotic behavior of the PDF is similar to the gas phase variables. At first, the PDF is spread around the value corresponding to the initial conditions. Then, the PDF tends to a Dirac function when the system is close to the equilibrium state.

Large dispersion of the vapor mass fraction is observed in the first PDFs due to a wide range of interface temperatures. Moreover, the mean vapor mass fraction moves toward its value at equilibrium ($Y_{vs}^* = 1$) in the successive instants. In contrast, the dispersion decreases due to the homogenization of the interface temperature, resulting in the increase of the PDF peak with time.

Comparing Figures 13a and 13b, while the general trend is similar as the system approaches equilibrium, a difference in PDF behavior is observed early in the simulation. In case 2 there is an initial increase in the mean value of Y_{vs}^* followed by a successive decrease. On the contrary, in case 1, the mean value of Y_{vs}^* decreases from the beginning of the simulation to the end. This initial increase of Y_{vs}^* in the second case could be attributed to the pressure drop of the system, which has the tendency to increase the vapor molar fraction (see equation 11).

The PDFs of the evaporation rate for the four studied times are presented in Figure 14 for both cases. In this context, the PDF is expected to evolve to a Dirac function shape at $\dot{\omega} = 0$ when the system reaches equilibrium. An important dispersion of the evaporation rate is observed at the earlier moments due to the high temperature and vapor mass fraction gradients. In addition, a significant asymmetry is observed in all PDFs with a peak on the left side and a long tail to the right, showing the low probability of the highest values of the evaporation rate. For successive instants, the decrease of the mean evaporation rate and the tail width is observed, causing an increase of the PDF peak. The main difference between both cases is that the magnitude of $\dot{\omega}$ is more significant in case 1.

Compared to the interface vapor mass fraction, the evaporation rate also depends on the interface temperature, but it also depends on the vapor concentration around the interface, and the interface geometry, such as the curvature

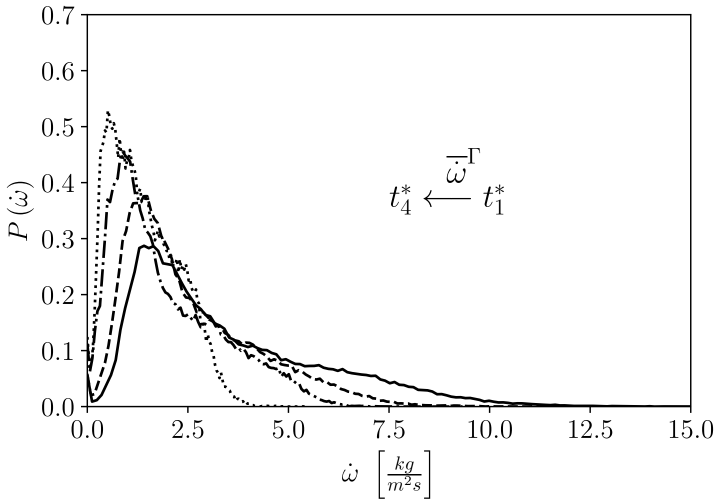

(a)

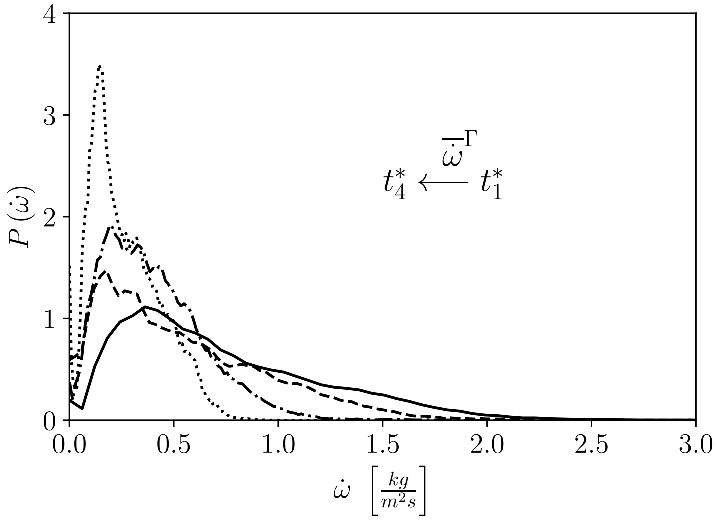

(b)

Figure 14: Instantaneous PDFs of $\dot{\omega}$ at t_1^* (solid line), t_2^* (dashed line), t_3^* (dashed-dotted line) and t_4^* (dotted line) for case 1 (a) and case 2 (b).

and characteristic lengths of the liquid and gas structure.

5.3. Influence of mean curvature on the evaporation rate

To better understand the simulation state at the studied times, the interface visualization colored by the evaporation rate magnitude for the same instants as the PDFs are presented in Figure 15. As for Figure 1, the effect of the turbulent velocity field on the interface deformations is observed. Moreover, the overall decrease of the evaporation rate as time passes is shown.

Figure 15 aims to understand the influence of the curvature on the evaporation rate. In this work, the convention represented in Figure 16 is used: red represents negative values of the mean curvature corresponding to a convex interface, and blue represents positive values of the mean curvature corresponding to a concave interface. In Figures 15, a decrease in the evaporation rate is observed when the interface is concave. Also, we can see some gas structures enclosed in the liquid and the low evaporation rate in these areas.

Figure 17 shows the joint PDF evolution of the evaporation rate $\dot{\omega}$ as a function of the normalized mean curvature H^*. Here, the mean curvature is normalized with the radius of the droplets used in the initialization of the HIT configuration for $\overline{\phi} = 0.1$ (see Luret et al. (2010); Canu et al. (2020) for more details). The joint PDFs are computed at the time instants corresponding to $\overline{Y}_v^* = 0.18, 0.32, 0.54$ and 0.72, and are presented in Figure 17 from left to right and from top to bottom. The first joint PDF (top left of Figure 17) represents the initial stages of the mixing process, and a wide dispersion of $\dot{\omega}$ over a large range of mean curvatures is observed. Additionally, $\dot{\omega}$ dispersion is related to the variations of local vapor concentration close to the interface, the interface deformations, and the diversity of liquid and gas structure characteristic lengths.

Similar observations were made by Scapin et al. (2021) for dispersed two-phase flow simulations in homogeneous shear turbulence. In their simulations, the liquid/gas interface and internal flow of the liquid droplets are resolved, and the evaporation rate depends on the vapor mass fraction and the temperature fields. Scapin et al. (2021) observed dispersion of $\dot{\omega}$ due to the interface deforma-

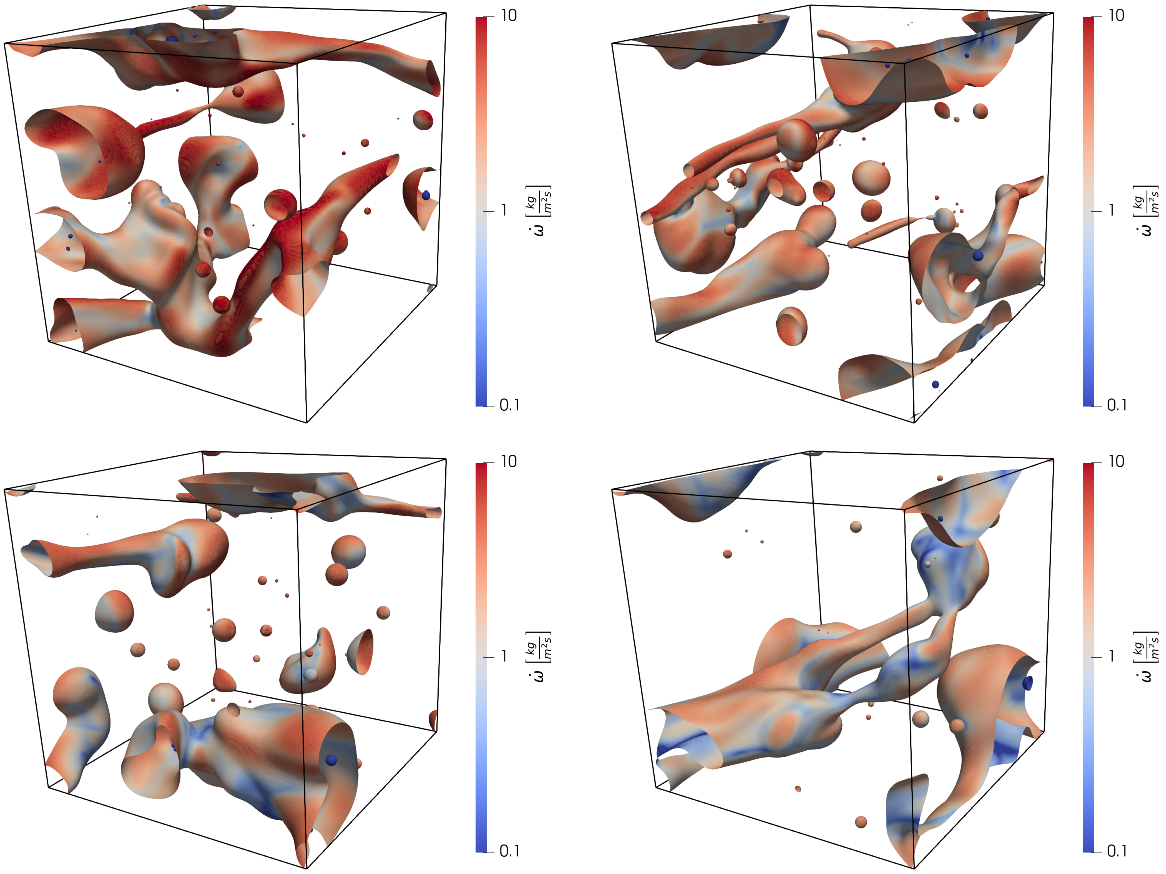

Figure 15: Instantaneous interface visualization (zero level set iso-contour) colored by the magnitude of the evaporation rate at t_1^*, t_2^*, t_3^* and t_4^* (from left to right, and top to bottom) for case 1.

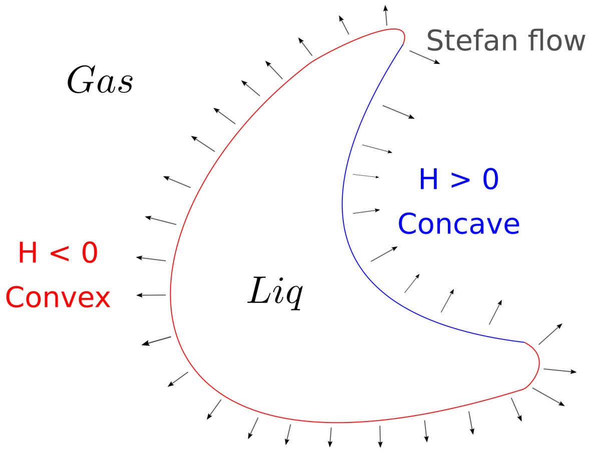

Figure 16: Graphical representation of the curvature sign of a deformed liquid structure.

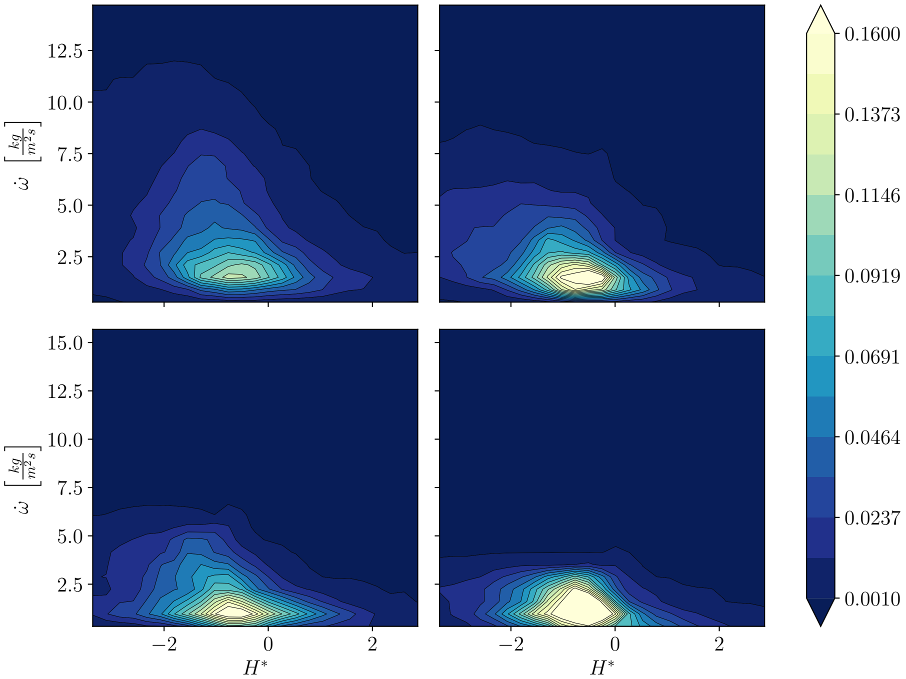

Figure 17: Instantaneous joint PDFs for $\dot{\omega}$ in function of the normalized curvature for case 1 at t_1^*, t_2^*, t_3^* and t_4^*.

tions and the non-homogeneity vapor concentration induced by the turbulent velocity field. Although, only values corresponding to a convex interface are presented because the interface deformation is relatively small, and there is no encapsulation of gas structures.

Furthermore, the larger values of the evaporation rate are found in the negative values of the mean curvatures. Hence, the probability of having a large evaporation rate is higher in small liquid structures than in the concave parts of the interface, usually present in gas structures. This could be explained by the formation of local saturation zones in concave interfaces. Indeed, the vapor generation is limited by the magnitude of the scalar gradient at the interface: in small gas structure the scalar generation is rapidly stopped when the gas structure is completely at saturation, which happens quickly if the gas structure is closed or quasi-closed. Consequently, the scalar gradient tends to zero, reducing the magnitude of the vaporization rate. Even if the gas structure is large and not saturated, local saturation can occurs in strongly curved concave interface region : the vapor is "trapped" and scalar gradients are greatly reduced as well as the vaporization rate. In the second joint PDF (top right of Figure 17), there is an increase in the probability of $\dot{\omega}$ in the negative values of the mean curvature (convex interface) whereas the probability is reduced in the positive curvature (concave interfaces), which indicates an increased saturation state close to concave interface as time evolve. Then, in the third joint PDF (bottom left of Figure 17), the decrease of $\dot{\omega}$ is more noticeable: the simulation is closer to the equilibrium state. Moreover, the values $\dot{\omega}$ are less dispersed because of the homogenization of the vapor mass fraction and temperature fields. Finally, in the last joint PDF (bottom right of Figure 17), the probability of both convex and concave interfaces start to become comparable, and the tendency of $\dot{\omega}$ to tend to zero is more evident.

In Figure 18, the temporal evolution of the joint PDF of the evaporation rate for case 2 is presented. Similar behavior to that shown in the Figure 17 is observed. However, the effects of the evaporation regime are easily seen. For example, the magnitude of the evaporation rate is considerably smaller, as

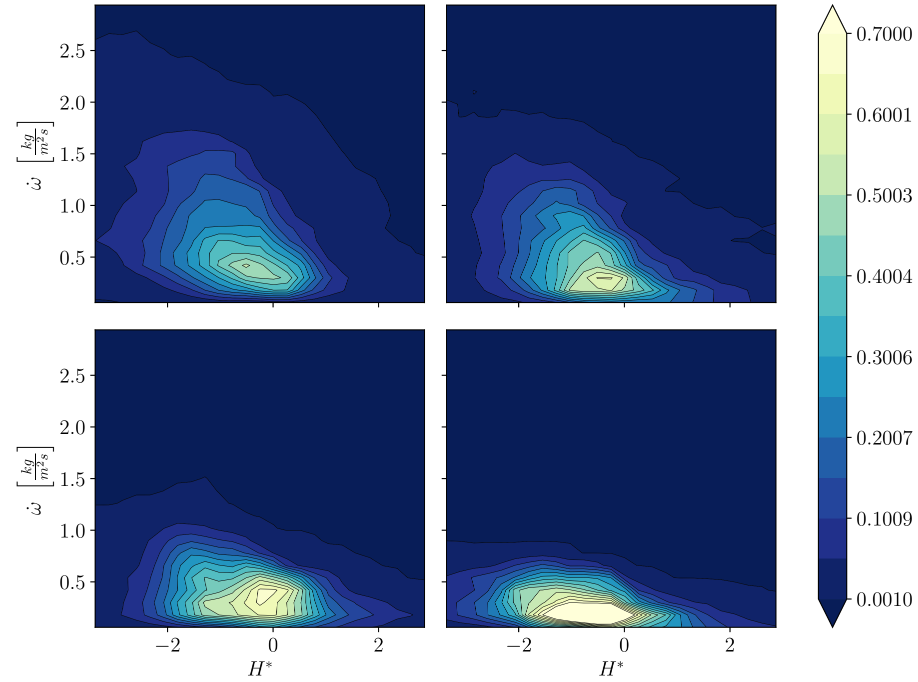

Figure 18: Instantaneous joint PDFs for $\dot{\omega}$ in function of the curvature for case 2 at t_1^*, t_2^*, t_3^* and t_4^*.

noted in the previous section (see Figure 4). In the earlier times, the shape of the joint PDFs for both cases is similar despite the difference in the magnitude of the evaporation rate. Once the turbulent mixing begins homogenizing the scalars, the differences in the joint PDFs become more apparent. For the same value of the mean vapor mass fraction, we can observe the flattened shape of the joint PDFs, which indicates a higher saturation level for the same value of the mean vapor mass fraction.

6. Conclusion

In this work, a fully compressible DNS formalism is applied to analyze the evaporation process and scalar turbulent mixing in an atomization regime. The method is able to capture the coupling between temperature, vapor mass fraction, and momentum conservation equations; resulting in a non-passive scalar mixing and a realistic representation of the vaporization process. Hence, our work is one of the few available in the literature that considers all these phenomena simultaneously.

The scalar turbulent mixing and the evaporation process are analyzed. To this end, the temporal evolution of the vapor mass fraction RMS for both cases is studied. An initial increase in the vapor mass fraction RMS results from the vapor production at the interface in a primarily dry air environment. Afterward, the scalar RMS decays as the equilibrium state is reached. Moreover, it was observed that the evaporation regime affects this behavior by increasing the maximum value when large evaporation rates are considered, and it is accompanied by a faster decay.

Furthermore, the temporal evolution of the PDFs of the vapor mass fraction is studied. It is shown that the PDFs shape strongly depends on the mixing stage, but remains close to a log normal distribution. An interesting behavior is observed in the right tail of the PDFs. Here, the shape of the PDFs tails depends on the vapor accumulation and generation near the interface. In addition, it is shown that the evaporation rate affects the temporal evolution of scalar PDFs;

resulting in an increased physical time to reach the equilibrium value of the vapor mass fraction when the evaporation rate decrease.

Finally, a statistical analysis of the surface averaged vapor mass fraction and evaporation rate is performed. The temporal evolution of their PDFs is analyzed. Both variables have shown a more significant dispersion in the first instants of the simulation. In the second case, the important pressure variation affects the vapor mass fraction generated at the interface: initially the PDFs means increase due to the pressure drop that enhances the scalar source, then a decrease is observed due to the lower scalar generation induced by lower temperatures in the system.

In addition, the behavior of the evaporation rate is studied from the curvature point of view, observing that the probability of the highest values of the evaporation rate is found in the convex interface curvatures. These results illustrate the impact of the assumptions typically made in the literature, where constant variables such as vapor mass fraction and evaporation rate are assumed at the interface. These assumptions appears to be not adequate in turbulent two-phase environments with high evaporation rates. Further work will be focus on improving vaporization modelling for dense two-phase flows, based on our DNS data.

7. Acknowledgements

This work was granted access to the HPC resources of IDRIS, TGCC, and CINES under the allocation (A0112B10101) made by GENCI (Grand Equipement National de Calcul Intensif). The CRIANN (Centre Regional Informatique et d'Applications Numeriques de Normandie) is also gratefully acknowledged (project No. 2017004) for its CPU resources. Also, the authors thank the MESCYT (Ministerio de Educación Superior, Ciencia y Tecnología, Dom. Rep.) and professor Bruno Renou who have supported and managed this work in the framework of the Caliope program.

References

Aslam, T.D., 2004. A partial differential equation approach to multidimensional extrapolation. Journal of Computational Physics 193, 349–355.

Bouali, Z., Duret, B., Demoulin, F.X., Mura, A., 2016. Dns analysis of small-scale turbulence-scalar interactions in evaporating two-phase flows. International Journal of Multiphase Flow 85, 326–335.

Bray, K., Champion, M., Libby, P., Swaminathan, N., 2006. Finite rate chemistry and presumed pdf models for premixed turbulent combustion. Combustion and Flame 146, 665–673.

Caltagirone, J.P., Vincent, S., Caruyer, C., 2011. A multiphase compressible model for the simulation of multiphase flows. Computers & fluids 50, 24–34.

Canu, R., Duret, B., Reveillon, J., Demoulin, F.X., 2020. Curvature-based interface resolution quality (irq) indicator to assess simulation accuracy. Atomization and Sprays 30.

Cengel, Y.A., Boles, M.A., Kanoğlu, M., 2011. Thermodynamics: an engineering approach. volume 5. McGraw-hill New York.

Chertkov, M., Falkovich, G., Kolokolov, I., 1998. Intermittent dissipation of a passive scalar in turbulence. Physical review letters 80, 2121.

Colin, O., Benkenida, A., 2003. A new scalar fluctuation model to predict mixing in evaporating two-phase flows. Combustion and Flame 134, 207–227.

Demoulin, F., Borghi, R., 2002. Modeling of turbulent spray combustion with application to diesel like experiment. Combustion and Flame 129, 281–293.

Di Battista, R., Bermejo-Moreno, I., Ménard, T., de Chaisemartin, S., Massot, M., 2019. Post-processing of two-phase dns simulations exploiting geometrical features and topological invariants to extract flow statistics: application to canonical objects and the collision of two droplets, in: International Conference on Multiphase Flow.

Dimotakis, P.E., 2005. Turbulent mixing. Annu. Rev. Fluid Mech. 37, 329–356.

Dodd, M.S., Mohaddes, D., Ferrante, A., Ihme, M., 2021. Analysis of droplet evaporation in isotropic turbulence through droplet-resolved dns. International Journal of Heat and Mass Transfer 172, 121157.

Duret, B., 2013. Simulation numérique directe des écoulements liquide-gaz avec évaporation: application à l'atomisation. Ph.D. thesis. Rouen, INSA.

Duret, B., Canu, R., Reveillon, J., Demoulin, F., 2018. A pressure based method for vaporizing compressible two-phase flows with interface capturing approach. International Journal of Multiphase Flow 108, 42–50.

Duret, B., Luret, G., Reveillon, J., Ménard, T., Berlemont, A., Demoulin, F.X., 2012. Dns analysis of turbulent mixing in two-phase flows. International Journal of Multiphase Flow 40, 93–105.

Eckart, C., 1948. An analysis of the stffiring and mixing processes in incompressible fluids .

Esmaeeli, A., Tryggvason, G., 2004. A front tracking method for computations of boiling in complex geometries. International Journal of Multiphase Flow 30, 1037–1050.

Eswaran, V., Pope, S., 1988. Direct numerical simulations of the turbulent mixing of a passive scalar. The Physics of fluids 31, 506–520.

Fedkiw, R.P., Aslam, T., Xu, S., 1999. The ghost fluid method for deflagration and detonation discontinuities. Journal of Computational Physics 154, 393–427.

de Frahan, M.T.H., Yellapantula, S., King, R., Day, M.S., Grout, R.W., 2019. Deep learning for presumed probability density function models. Combustion and Flame 208, 436–450.

Fuster, D., Popinet, S., 2018. An all-mach method for the simulation of bubble dynamics problems in the presence of surface tension. Journal of Computational Physics 374, 752–768.

Gerlinger, P., 2003. Investigation of an assumed pdf approach for finite-rate chemistry. Combustion Science and Technology 175, 841–872.

Germes Martinez, L.A., 2022. Direct Numerical Simulation of turbulent liquid/gas compressible flows with phase change. Ph.D. thesis. Normandie Université.

Girimaji, S., 1991. Assumed β-pdf model for turbulent mixing: Validation and extension to multiple scalar mixing. Combustion Science and Technology 78, 177–196.

Hunt, J., 1985. Turbulent diffusion from sources in complex flows. Annual review of fluid mechanics 17, 447–485.

Ishii, M., Hibiki, T., 2010. Thermo-fluid dynamics of two-phase flow. Springer Science & Business Media.

Jayawickrama, T.R., Haugen, N.E.L., Babler, M.U., Chishty, M., Umeki, K., 2021. The effect of stefan flow on nusselt number and drag coefficient of spherical particles in non-isothermal gas flow. International Journal of Multiphase Flow , 103650.

Jayawickrama, T.R., Haugen, N.E.L., Babler, M.U., Chishty, M.A., Umeki, K., 2019. The effect of stefan flow on the drag coefficient of spherical particles in a gas flow. International Journal of Multiphase Flow 117, 130–137.

Jayesh, Warhaft, Z., 1992. Probability distribution, conditional dissipation, and transport of passive temperature fluctuations in grid-generated turbulence. Physics of Fluids A: Fluid Dynamics 4, 2292–2307.

Juneja, A., Pope, S., 1996. A dns study of turbulent mixing of two passive scalars. Physics of Fluids 8, 2161–2184.

Lempke, M., Keller, R., Gerlinger, P., 2015. Influence of spatial discretization and unsteadiness on the simulation of rocket combustors. International journal for numerical methods in fluids 79, 437–455.

Lipatnikov, A.N., Nilsson, T., Yu, R., Bai, X.S., Sabelnikov, V.A., 2021. Assessment of a flamelet approach to evaluating mean species mass fractions in moderately and highly turbulent premixed flames. Physics of Fluids 33, 045121.

Lockwood, F., Naguib, A., 1975. The prediction of the fluctuations in the properties of free, round-jet, turbulent, diffusion flames. Combustion and Flame 24, 109–124.

Luret, G., Menard, T., Berlemont, A., Reveillon, J., Demoulin, F.X., Blokkeel, G., 2010. Modeling collision outcome in moderately dense sprays. Atomization and Sprays 20.

Malan, L., 2018. Direct numerical simulation of free-surface and interfacial flow using the VOF method: cavitating bubble clouds and phase change. Ph.D. thesis. University of Cape Town.

Martinez, L.G., Duret, B., Reveillon, J., Demoulin, F., 2021. A new dns formalism dedicated to turbulent two-phase flows with phase change. International Journal of Multiphase Flow 143, 103762.

Mohamed, E., Florence, D., Adam, L., Thibault, M., Marc, M., et al., 2019. Statistical modeling of the gas–liquid interface using geometrical variables: toward a unified description of the disperse and separated phase flows. International Journal of Multiphase Flow 120, 103084.

Ménard, T., Tanguy, S., Berlemont, A., 2007. Coupling level set/VOF/ghost fluid methods: Validation and application to 3d simulation of the primary break-up of a liquid jet. International Journal of Multiphase Flow 33, 510–524.

Overholt, M., Pope, S., 1996. Direct numerical simulation of a passive scalar with imposed mean gradient in isotropic turbulence. Physics of Fluids 8, 3128–3148.

Palmore Jr, J., Desjardins, O., 2019. A volume of fluid framework for interface-resolved simulations of vaporizing liquid-gas flows. Journal of Computational Physics 399, 108954.

Pumir, A., Shraiman, B.I., Siggia, E.D., 1991. Exponential tails and random advection. Physical review letters 66, 2984.

Reveillon, J., Bray, K., Vervisch, L., 1998. Dns study of spray vaporization and turbulent micro-mixing, in: 36th AIAA Aerospace Sciences Meeting and Exhibit, p. 1028.

Reveillon, J., Demoulin, F.X., 2007. Effects of the preferential segregation of droplets on evaporation and turbulent mixing. Journal of Fluid Mechanics 583, 273–302.

Reveillon, J., Vervisch, L., 2000. Spray vaporization in nonpremixed turbulent combustion modeling: a single droplet model. Combustion and flame 121, 75–90.

Salehi, M., Bushe, W., 2010. Presumed pdf modeling for rans simulation of turbulent premixed flames. Combustion Theory and Modelling 14, 381–403.

Scapin, N., Barba, F.D., Lupo, G., Rosti, M.E., Duwig, C., Brandt, L., 2021. Finite-size evaporating droplets in weakly-compressible homogeneous shear turbulence. arXiv preprint arXiv:2104.10184 .

Scapin, N., Costa, P., Brandt, L., 2020. A volume-of-fluid method for interface-resolved simulations of phase-changing two-fluid flows. Journal of Computational Physics 407, 109251.

Shraiman, B.I., Siggia, E.D., 1994. Lagrangian path integrals and fluctuations in random flow. Physical Review E 49, 2912.

Tanguy, S., Ménard, T., Berlemont, A., 2007. A level set method for vaporizing two-phase flows. Journal of Computational Physics 221, 837–853.

Tavoularis, S., Corrsin, S., 1981. Experiments in nearly homogenous turbulent shear flow with a uniform mean temperature gradient. part 1. Journal of Fluid Mechanics 104, 311–347.

Urbano, A., Bibal, M., Tanguy, S., 2022. A semi implicit compressible solver for two-phase flows of real fluids. Journal of Computational Physics 456, 111034.

Yeung, P., 2001. Lagrangian characteristics of turbulence and scalar transport in direct numerical simulations. Journal of fluid mechanics 427, 241–274.

Yeung, P., Donzis, D., Sreenivasan, K., 2005. High-reynolds-number simulation of turbulent mixing. Physics of Fluids 17, 081703.

Yeung, P., Sreenivasan, K., 2013. Spectrum of passive scalars of high molecular diffusivity in turbulent mixing. Journal of Fluid Mechanics 716.

Yeung, P., Sreenivasan, K., 2014. Direct numerical simulation of turbulent mixing at very low schmidt number with a uniform mean gradient. Physics of Fluids 26, 015107.

Yeung, P., Xu, S., Sreenivasan, K., 2002. Schmidt number effects on turbulent transport with uniform mean scalar gradient. Physics of Fluids 14, 4178–4191.